



*Facultad
de
Ciencias*

**Estudio espectroscópico del Gd_2O_2S
impurificado con Er^{3+}**

(Spectroscopic study of Er^{3+} -doped Gd_2O_2S)

Trabajo de Fin de Grado
para acceder al

GRADO EN FÍSICA

Autor: Inés Temiño Gutiérrez

Director: Rafael Valiente Barroso

Septiembre - 2013

Dr. Rafael Valiente Barroso, Profesor Titular de Física Aplicada

INFORMA:

Que el trabajo que se presenta en esta memoria, titulado “ *Estudio espectroscópico del Gd_2O_2S impurificado con Er^{3+}* ”, ha sido realizado bajo mi dirección en el DEPARTAMENTO DE FÍSICA APLICADA de la Facultad de Ciencias de la UNIVERSIDAD DE CANTABRIA dentro del programa oficial de Grado en Física y emito mi conformidad para que dicha Memoria sea presentada y tenga lugar, posteriormente, la correspondiente Lectura y Defensa.

Santander, Septiembre de 2013

Fdo. Rafael Valiente Barroso

Abstract

The main goal of this work is the spectroscopic characterization of a microcrystalline powdered sample of $\text{Gd}_2\text{O}_2\text{S}:\text{Er}^{3+}$ (10%). A complete study of its optical properties has been done, focusing on NIR to VIS up-conversion (UC) phenomena.

In general, oxysulfides activated with trivalent rare earth ions have shown to be phosphors with high luminescence efficiency. In particular, 10% Er^{3+} is the optimum concentration to achieve the highest UC efficiency with Er^{3+} -doped gadolinium oxysulfide upon 1510 nm excitation. Up-conversion emission spectra were obtained under 980 nm excitation at different temperatures from 10 K to 300 K. Also, multi-up-conversion luminescence was observed: blue, green and red emission under excitation into five different Er^{3+} excited states, which had never been observed before in any UC material.

The temporal evolution of UC luminescent emission under different excitation energies was also measured, which enabled us to identify the dominant UC mechanism, simultaneous multi-photon absorption or energy transfer processes.

In addition, Raman and reflectance spectroscopy has been used in order to study both the host material and the dopant ion. As a result, we determined the appropriate wavelength at which Er^{3+} emission can be excited and also the maximum phonon energy of the lattice.

The determination of the magnitude of the crystal-field splitting of two Er^{3+} excited states, $^4S_{3/2}$ and $^4F_{9/2}$, and the ground state, $^4I_{15/2}$, was achieved through the study of the temperature dependence of excitation and emission spectra.

Index

1	INTRODUCTION.....	1
1.1	Rare-earth ions.....	1
1.1.1	The energy levels: crystal-field theory.....	1
1.1.2	The Dieke diagram.....	3
1.2	Electronic transitions.....	5
1.2.1	Selection rules and Judd-Ofelt theory.....	5
1.2.2	Temporal evolution of luminescence.....	5
1.3	Non-radiative electronic transitions.....	6
1.3.1	Multi-phonon relaxation: the energy-gap law.....	7
1.3.2	Energy transfer processes.....	7
1.4	Up-conversion phenomena.....	8
1.5	Gd ₂ O ₂ S: Er ³⁺	10
1.5.1	State of the art.....	11
2	EXPERIMENTAL.....	12
2.1	Diffuse reflectance.....	12
2.2	Excitation and luminescence.....	13
2.3	Lifetime measurements.....	15
2.4	Low temperature measurements.....	16
2.5	Raman.....	17
3	RESULTS AND DISCUSSION.....	18
3.1	Dopant and host characterization.....	18
3.1.1	Erbium ions energy levels.....	18
3.1.2	Raman spectrum.....	19
3.2	Excitation and emission of Er ³⁺ -doped Gd ₂ O ₂ S.....	20
3.2.1	Excitation spectra.....	20
3.2.2	Temperature dependence of the emission intensity.....	21
3.2.3	Splitting of ⁴ I _{15/2} (g.s.), ⁴ F _{9/2} , and ⁴ S _{3/2} states - Stark levels.....	27
3.3	Up-conversion luminescence.....	30
3.3.1	Temperature dependence.....	30
3.3.2	Multi up-conversion.....	32
3.4	Lifetime of the erbium energy levels.....	35
3.4.1	Temperature dependence of the lifetime of some Er ³⁺ excited states.....	40
3.4.2	Rate equations.....	42
4	CONCLUSIONS.....	44
	References.....	45

1 INTRODUCTION

This work deals with optical properties of $\text{Gd}_2\text{O}_3\text{:Er}^{3+}$ (10%), from the temperature dependence of excitation and emission spectra to the splitting and lifetime of the energy levels, focusing on multi up-conversion luminescence.

In this section, the importance of up-conversion materials is shown, and the main features of rare earth ions that make them suitable for this purpose are presented. Here is also an introduction to the theoretical aspects concerning absorption and emission spectra, and energy transfer processes (especially up-conversion), which will allow the understanding of the experimental results.

1.1 Rare-earth ions

Since their discovery in the mid-1960s (by Auzel [1, 2] and Ovsyankin-Feofilov [3], independently), there has been much interest in materials that emit visible or even UV radiation when excited with infrared light and they have been extensively studied [4]. Due to this up-conversion (UC) luminescence they have been used in applications such as displays, lasers, or IR detectors; more recently, enhancing solar cells efficiency [4, 5] and biomedical applications (such as biolabeling, cancer therapy and nanothermometers [6,7, 8]) have attracted most of the attention.

In this sense, rare earth doped materials have been broadly studied as their energy levels spread over a wide range and there is more than one metastable state, which is the basic requirement for UC [9]. Thus, they are suitable for the multi-photon absorption and energy transfer processes that allow NIR to VIS/UV up-conversion.

1.1.1 The energy levels: crystal-field theory

Trivalent rare-earth ions (RE^{3+}) have an outer electronic configuration $5s^25p^64f^n$, where n represents the number of electrons in the unfilled shell, which varies from 1 (Ce^{3+}) to 13 (Yb^{3+}). The $4f^n$ valence electrons are spectroscopically active, and screened by the outer filled electronic shells.

This electronic configuration gives rise to an energy level structure that is determined by the Hamiltonian, since it includes all the possible different interactions. For the free ion (FI), three independent terms are usually considered and it is written as:

$$H_{FI} = H_0 + H_{ee} + H_{SO} \quad (1)$$

where:

- H_0 is the central-field Hamiltonian (kinetic and potential energy), which reflects the electrostatic potential acting on the valence electrons due to the nucleus and closed-shell electrons;
- H_{ee} considers the repulsive Coulomb interactions among the valence electrons;
- H_{SO} , which has a relativistic origin, takes into account the spin-orbit interaction (between the spin and the angular momentum of the electron, s and l) summed over these electrons. [10]

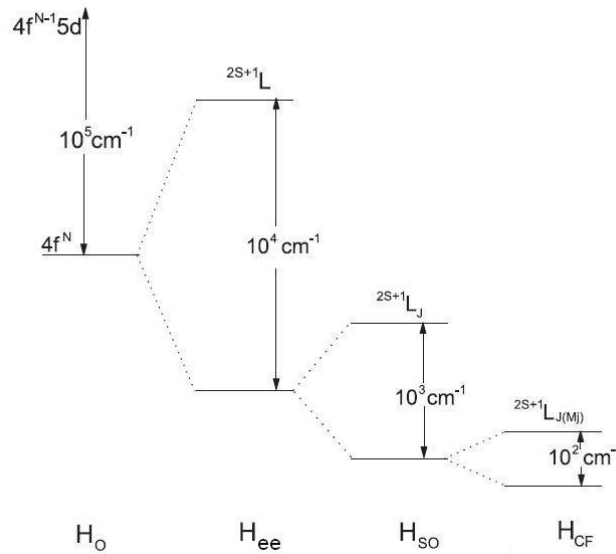


Figure 1.1: Schematic representation and order of magnitude of the distinct contributions of the Hamiltonian (Coulomb interaction (H_{ee}), spin-orbit coupling (H_{SO}) and crystal-field effect (H_{CF})) to the energy level splitting for rare earth ions. Ref. [11].

In the case of RE ions the relative strength for these interactions is: $H_0 \gg H_{ee}, H_{SO}$. The magnitude of the H_{ee} and H_{SO} interactions is similar, which strictly corresponds to an intermediate case between LS and jj coupling. However, this is simplified by considering the *Russell-Saunders approximation* (LS coupling, $H_{ee} > H_{SO}$). As a result, the electronic states are labeled as $^{2S+1}L_J$ multiplets, using the total quantum numbers S (spin), L (orbital angular momentum), and $J = L + S$ (total angular momentum).

When ions are incorporated in a material the effect of the lattice must be considered, and this is done by adding another term to the Hamiltonian, H_{CF} , the crystal-field interaction, then:

$$H = H_{FI} + H_{CF} \quad (2)$$

Because of the mentioned shielding effect in RE^{3+} , the magnitude of the CF interaction on RE^{3+} is much smaller than that of the previous interactions (Fig. 1.1). Thus, when they are incorporated in crystals as trivalent cations, the f-f transitions are weakly affected by the presence of the next nearest neighbors. Therefore, the *weak crystal-*

field approach is the appropriate scenario. This is also known as the weak crystal-field coupling case, which means small ion-lattice interactions [12].

In this case perturbation theory is applied, H_{CF} being the perturbation Hamiltonian over the $^{2S+1}L_J$ states. Consequently, the free ion energy levels are only slightly perturbed (shifted and split) by the crystal field while the spin-orbit interaction still dominates (Fig. 1.1).

As a result, the absorption and emission spectra show very similar patterns of sharp peaks independently of the host material, and also similar to the free ion spectrum. This means that transitions between electronic energy multiplets of the $4f^n$ electronic configuration of the RE^{3+} ions (intraconfigurational or f-f transitions) are usually responsible for the optical properties in the material. Although interconfigurational or f-d transitions are far more intense, they are usually observed in the UV or VUV region.

1.1.2 The Dieke diagram

The *Dieke diagram*, in Fig. 1.2, shows the approximate energy of the $^{2S+1}L_J$ states for the RE^{3+} ions in $LaCl_3$ [13]. For this reason, it is the key to interpreting the absorption and luminescence spectra. Although the width and the center of gravity of the energy levels can slightly change, absorption and emission peaks can be assigned by comparison of the spectrum obtained with this diagram. We have studied the optical spectroscopic properties of Er^{3+} -doped Gd_2O_2S , with electronic configuration $[Xe] 4f^{11}$.

The number of energy levels for a rare earth ion (number of microstates of the system) is given by:

$$N = \binom{14}{n} \quad (3)$$

Where 14 is the maximum number of electrons in the $4f^n$ shell and n is the actual number of electrons for a particular ion. That is, for $n = 11$ (Er^{3+}) there are 364 microstates.

All these energy levels only appear with different energy when considering splitting due to both Stark and Zeeman effects. Otherwise they are grouped in degenerated $^{2S+1}L_J$ multiplets, and their degeneracy is $2J + 1$.

However, for half-integer J (or odd n , like Er^{3+}), the crystal field makes each $^{2S+1}L_J$ multiplet split in a maximum number of components given by $J + 1/2$ (*Kramers' theorem*, refs. [14, 15]). This leads to a maximum of 8 Krammer doublets for the Er^{3+} ground state, $^4I_{15/2}$. The actual magnitude of the crystal-field splitting and the number of *Stark sublevels* is determined by the host, that is, the local symmetry around the optically active center. It is possible to identify these components by studying the low temperature excitation and emission spectra, since in that case overlap between transitions to or from different sublevels is avoided (hot bands). However, the assignment of these levels to the corresponding Stark levels would require theoretical calculations and the use of polarization measurements. In our case, it was impossible to carry this out due to the lack of an appropriated single crystal.

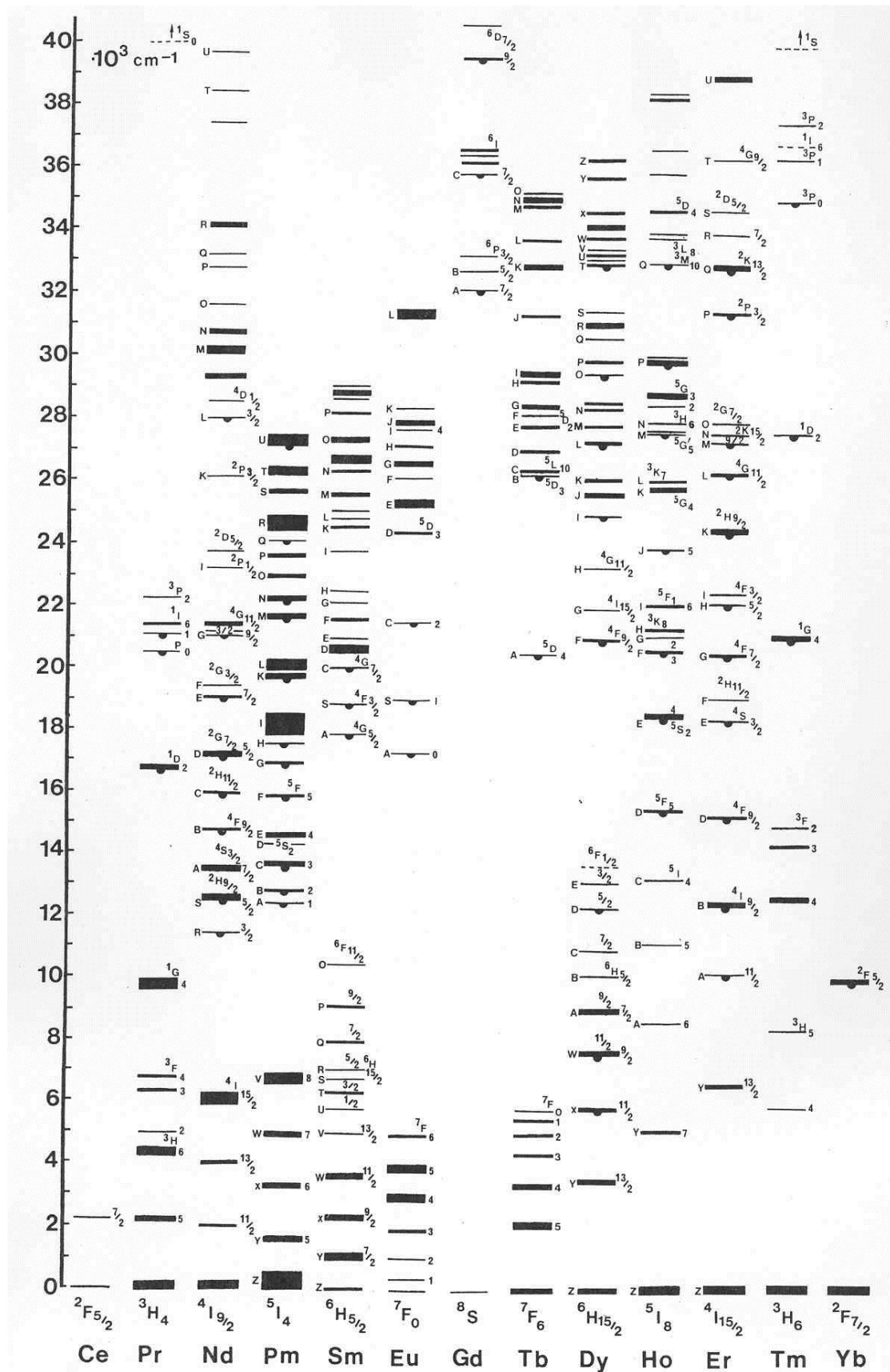


Figure 1.2: Dieke diagram, showing the energy of the $^{2S+1}L_J$ states for the RE^{3+} ions in $LaCl_3$ [13]. The width of these states is related to the energy splitting caused by the crystal field.

1.2 Electronic transitions

Dopant ions in a material can provide energy levels within the energy gap of the host crystal in such a way that they give rise to optical transitions of energy lower than the absorption edge of the host.

When a sample is illuminated, absorption takes place if the light frequency is resonant with a transition between two states, where the energy of the final state is higher than that of the initial state (generally the ground state). Then, relaxation from an excited energy level can happen both by a radiative or non-radiative process. The former case is known as photoluminescence and spontaneous emission of light is observed.

1.2.1 Selection rules and Judd-Ofelt theory

According to *Fermi's golden Rule*, the probability of a transition to take place is proportional to the matrix element and the density of modes:

$$W_{i \rightarrow f} \propto |\langle i | H_{int} | f \rangle|^2 \rho(\nu) \quad (4)$$

where H_{int} represents the Hamiltonian of the radiation-matter interaction, $|i\rangle$ and $|f\rangle$ are the initial and final states, and $\rho(\nu)$ is the density of modes of frequency ν .

The Hamiltonian has different terms that correspond to different possible mechanisms. The electric dipole term (ED) is the most important one in comparison with the magnetic dipole (MD) and electric quadrupole (EQ) terms. Transitions through the ED mechanism are allowed if the initial and final states have opposite parity, $(-1)^l$, because H_{ED} is an odd parity operator (*Laporte's selection rule*). Hence, for rare-earth ions all f-f transitions are parity forbidden and they should be weakly observed. However, very intense lines are found in their spectra, which means that most of the transitions occur at the electric dipole order.

This ED allowance is explained by the *Judd-Ofelt theory* [16], which considers the mixture of states from the $4f^n$ and $4f^{n-1} 5d$ electronic configurations (with opposite parity). This can happen only if the symmetry group of the crystal field lacks the inversion center or thanks to vibrational modes of odd symmetry (which destroys the inversion symmetry).

As a result, the general rule to observe an intraconfigurational transition in rare earth ions is:

$$|\Delta J| \leq 6 \quad (5)$$

With the exception of the $J = 0 \leftrightarrow J' = 0$ transition, which is strictly forbidden.

1.2.2 Temporal evolution of luminescence

Under continuous excitation there is a constant spontaneous emission of light, which corresponds to the steady state. On the contrary, under modulated excitation there is a temporal evolution of the excited state population and the emitted light intensity follows an exponential decay:

$$I_{em}(t) = I_0 e^{-A_t t} \quad (6)$$

where $I_0 = I_{em}(0)$ is the emission intensity just after the pulse of light has been absorbed and the center has been excited. A_t is the total decay probability, taking into account the radiative rate (A_r) and the non-radiative rate (A_{nr}):

$$A_t = A_r + A_{nr} \quad (7)$$

This can be rewritten in terms of the lifetime, given by $\tau = 1/A_t$, which represents the mean time it takes the atoms to de-excite or the time after which emitted light intensity (and the excited state population) decreases by a factor $1/e$.

$$I_{em}(t) = I_0 e^{-t/\tau} \quad (8)$$

$$\frac{1}{\tau} = \frac{1}{\tau_r} + A_{nr} \quad (9)$$

For trivalent lanthanides the time scale of this emission is typically between μs and ms , as expected for a parity-forbidden transition. Both the radiative and the non-radiative processes are considered since luminescence is proportional to the population of the excited state, which can decay in either way.

1.3 Non-radiative electronic transitions

In addition to light-emitting transitions (radiative de-excitation), there is another possible mechanism through which the center can relax to lower energy levels. There are two processes that compete with luminescence: multi-phonon relaxation and energy transfer, both of which help to diminish the population of an initially excited state. They differ in the number of centers involved, and also in the physical origin; while the former involves the creation of multiple phonons, the latter requires the overlap of emission and absorbance spectra.

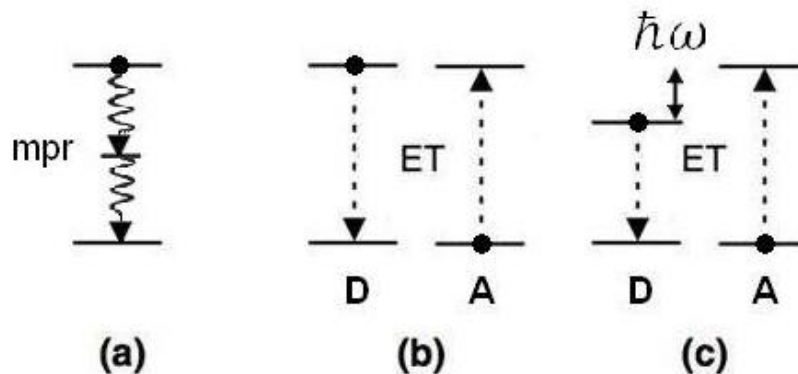


Figure 1.3: (a) Scheme for the multi-phonon relaxation (mpr) process. (b, c) Scheme for a resonant and a phonon-assisted energy transfer (ET) process, respectively. In the case presented, the absorption of a phonon is required. D and A label the donor and acceptor centers. (See section 1.3.2)

1.3.1 Multi-phonon relaxation: the energy-gap law

When multi-phonon relaxation takes place, at least part of the excitation energy is transformed into vibrational energy in the host lattice, i.e. heat. This occurs through the emission of various phonons instead of one photon. The typical time scale for this process is around femtoseconds.

In the case of rare-earth ions, the rate for a non-radiative transition through multi-phonon relaxation (mpr) is given by the *energy-gap law* [9, 17]. It basically states that the non-radiative rate, A_{nr} , of a particular excited state is strongly related to the energy separation ΔE between this state and the one just below it.

The probability of this process decreases exponentially with an increasing energy gap due to the fact that more phonons are involved. Considering the highest-energy vibration for the crystal, $\hbar\omega_{max}$, the amount of phonons that are needed to bridge the gap between two consecutive states is known as the reduced energy gap (Fig. 1.3(a)):

$$p = \Delta E / \hbar\omega_{max} \quad (10)$$

Thus:

$$W_{nr}(mpr) \propto e^{-ap} \quad (11)$$

where a is a constant that depends on the host material.

In other words, as the number of phonons p increases, relaxation by multi-phonon emission is less probable and luminescence dominates. This process is competitive if $p \leq 6$.

1.3.2 Energy transfer processes

These processes involve two or more optically active centers, since all or part of the energy of an excited center D (called donor or sensitizer) is transmitted to a second nearby center A (called acceptor or activator). The de-excitation of the donor, $D^* \rightarrow D$, and the excitation of the acceptor, $A \rightarrow A^*$, occur simultaneously and no photons are emitted in the transfer process (this is a non-radiative mechanism).

Energy transfer can be induced by electric multipolar interactions (Förster theory) or exchange interactions (Dexter theory) [17, 18]. Also, this transference can occur between donors and acceptors that are identical, if it is a singly-doped or high concentrated material, or different, if there is more than one kind of dopant ion. This is often referred to as energy *migration* and energy transfer, respectively (Fig. 1.4). Energy transfer processes strongly depend on the donor-acceptor distance and therefore are concentration dependent.

The probability for energy transfer (ET) can be written as follows:

$$W_{nr}(ET) \propto \int g_D(E)g_A(E)dE \quad (12)$$

This factor is called the *spectral overlap integral*, and $g_D(E)$ and $g_A(E)$ are the normalized emission and absorption lineshape functions. It is in fact needed for energy conservation, being a maximum when the donor and the acceptor have coincident

energy levels. In this case the process is *resonant*. On the other hand, *phonon-assisted* energy transfer processes take place when there is an energy mismatch, something usual for centers that are different. Both cases are shown in Fig. 1.3(b, c), in particular a phonon-assisted process that requires the absorption of a phonon.

Rare-earth ions have shown to be very suitable for energy transfer processes since they often have a multitude of metastable excited states. Some energy transfer processes are energy migration, which requires a sequence of energy transfer steps before the excitation reaches the emission center or quenching center (killer), and cross relaxation (CR), which consists on the population of an intermediate excited energy level through an ET process. Among these, we will focus on the up-conversion (UC) process in the following section. Fig. 1.4 shows UC is the opposite process of CR.

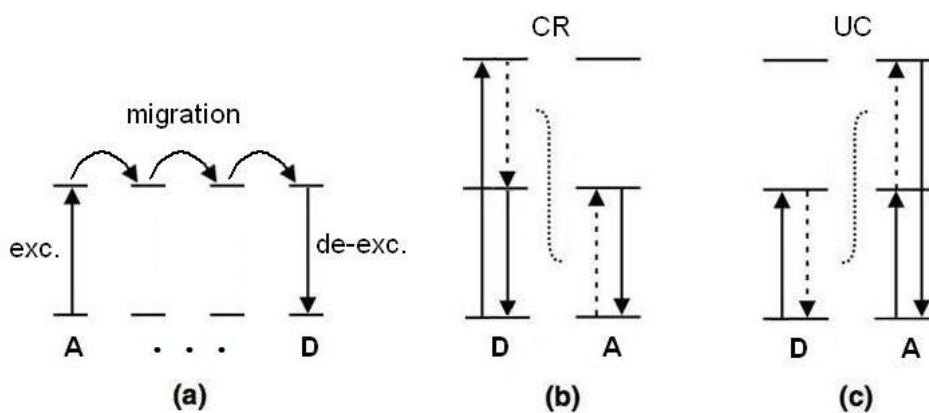


Figure 1.4: Scheme of different processes based on energy transfer: (a) energy migration, (b) cross relaxation, and (c) up-conversion.

1.4 Up-conversion phenomena

The result of up-conversion processes is the population of highly excited states after the absorption of two or more low energy photons, which may then lead to the emission of a higher energy photon. Then, NIR incident radiation can be converted into visible or even UV light.

In the case of RE^{3+} -doped materials this happens through real intermediate metastable states [9, 19], which act as an energy reservoir to make possible multi-photon absorption and/or energy transfer mechanisms. In $\text{Gd}_2\text{O}_2\text{S: Er}^{3+}$, there are basically two types of up-conversion processes, GSA/ESA and GSA/ETU, or briefly ESA and ETU [18].

In ETU, an excited ion non-radiatively transfers its energy to another excited neighboring ion. Ground state absorption (GSA) is followed by energy transfer up-conversion.

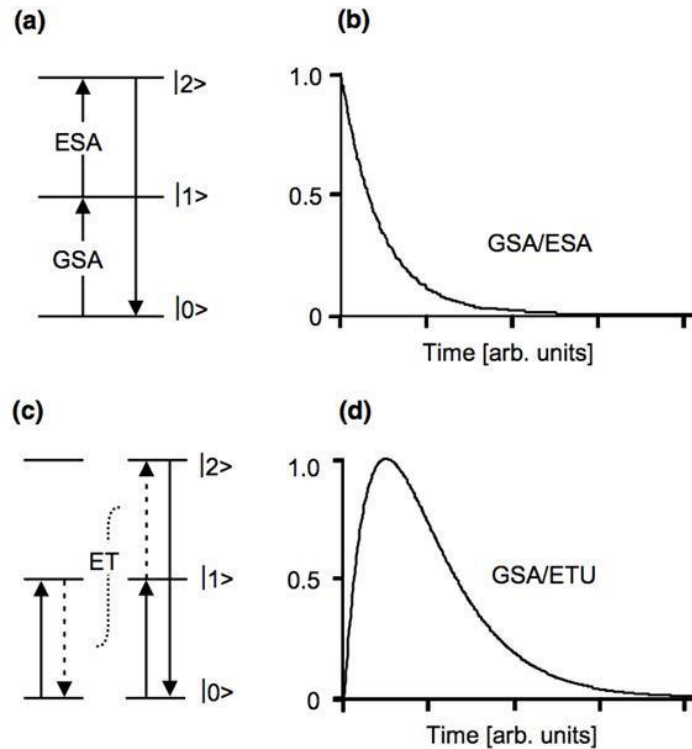


Figure 1.5: (a) Scheme of GSA/ESA process. (b) Temporal evolution of luminescence for GSA/ESA showing a direct exponential decay. (c) Scheme of GSA/ETU process through energy transfer (ET). (d) Time dependence of luminescent emission for GSA/ETU showing a rise followed by a decay. Refs. [5, 9].

In ESA, two consecutive photon absorptions (ground state absorption/excited state absorption) can take place. In case of a pulsed light source, absorption of the two photons should take place during the same pulse.

In Fig. 1.5 a schematic illustration shows how these up-conversion processes take place. In both cases resonance is a crucial factor; it is important that the energy involved in the second step is close to that of the incident light (in case of ESA) or to the gap between two states of a nearby ion (in case of ETU). For this reason, an energy matching level structure is key for UC to occur.

We should note that although high phonon energies make luminescence less competitive, phonons play an important role in making the UC process efficient. Phonon assistance is required for both the ETU and ESA mechanisms as an energy mismatch can be made up by phonon absorption or emission.

The temporal evolution of luminescence when using short pulsed excitation (in the ns range) allows us to distinguish between ESA and ETU processes. The first mechanism must occur during the light pulse, whereas the ETU process can continue after the short pulsed excitation. As a result, while ESA is characterized by a pure exponential decay after an instantaneous rise, ETU shows a rise followed by a decay, i.e. the emitting state is populated after the pulse through an efficient energy transfer process. This can be seen in Fig. 1.5(b, d), where $t = 0$ is the instant just after the pulse of light.

1.5 Gd₂O₂S: Er³⁺

The oxysulfide Gd₂O₂S has a hexagonal structure, which is shown in Fig. 1.6 using the lattice parameters from ref. [20]. The symmetry is trigonal and the space group is $P\bar{3}m1$. In the doped material, Er³⁺ ions replace Gd³⁺ ions and they are surrounded by four oxygen and three sulfur ions, forming a seven coordinated geometry. Refs. [4, 19].

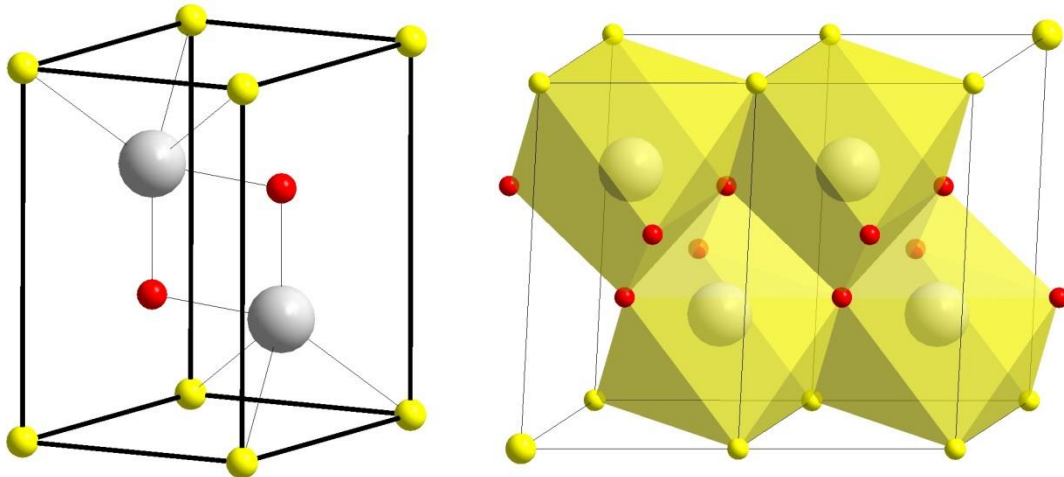


Figure 1.6: Gd₂O₂S crystalline structure and coordination polyhedra.

It is known that cationic radii depends on the coordination number. Considering that Er³⁺ ions replace Gd³⁺ ions in the sevenfold-coordination found in the oxysulfides, it is estimated [21] that both have similar ionic radii: $R(\text{Er}^{3+})=0.92\text{\AA}$ and $R(\text{Gd}^{3+})=0.98\text{\AA}$. Due to this similarity doping produces little distortion of the lattice.

The crystalline structure was confirmed by X-ray diffraction (XRD). The peak positions of the diffraction pattern of the Gd₂O₂S: Er³⁺(10%) sample match with those of the trigonal phase of the oxysulfide. The comparison is presented in Fig. 1.7(a). High resolution scanning electron microscopy (SEM) was used to check the size and morphology of the sample. Fig. 1.7(b) shows that the crystallite size is around 2-10 μm and the sample has uniform and well-separated particles [4].

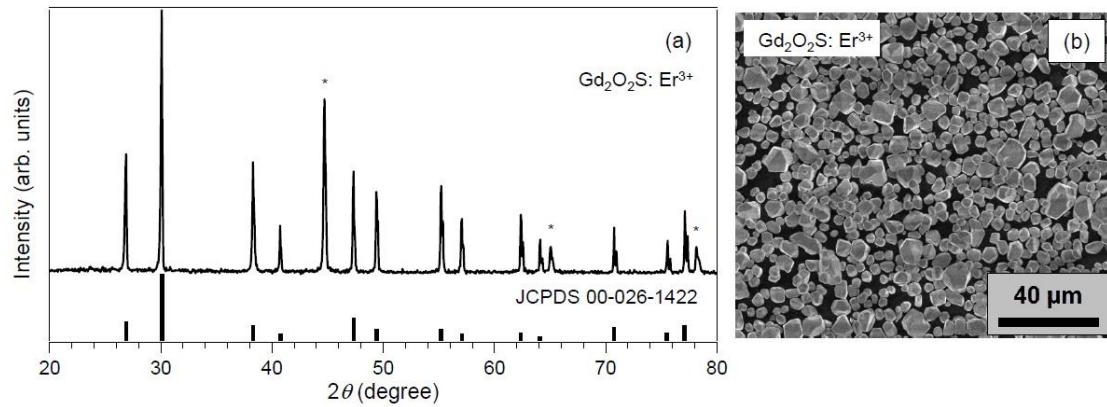


Figure 1.7: (a) $\text{Gd}_2\text{O}_2\text{S}: 10\% \text{Er}^{3+}$ XRD pattern and (b) SEM micrograph of $\text{Gd}_2\text{O}_2\text{S}: 10\% \text{Er}^{3+}$. * in (a) indicate peaks corresponding to the Al substrate. Ref. [4].

1.5.1 State of the art

As we have shown, RE^{3+} are very suitable for up-conversion materials. In particular, Er^{3+} is especially attractive since it has a great number of energy levels due to its electronic configuration, and they are almost equidistant.

The quantity which measures the competition between radiative and non-radiative processes is quantum efficiency, which is the ratio of the number of emitted photons versus the absorbed photons. One of the key requirements for an efficient IR to VIS up-conversion is that the host material possesses low energy phonon modes [19], so that radiative decay will dominate. Among many possible hosts, oxysulfides activated with trivalent rare earth ions, which have average phonon energy of 520 cm^{-1} [22], have shown high luminescence efficiency. In particular, 10% Er^{3+} has shown to be the optimum concentration to achieve the highest UC efficiency with Er^{3+} -doped gadolinium oxysulfide upon 1510 nm excitation [4].

2 EXPERIMENTAL

As we previously mentioned, the goal of this work is the characterization of $\text{Gd}_2\text{O}_2\text{S}:\text{Er}^{3+}$ through the study of its optical properties, focusing on up-conversion phenomena. It is important to stress that the synthesis of the sample has not been part of the process; on the contrary, the material was obtained by Leuchtstoffwerk Breitung GmbH and then delivered to Cantabria's University thanks to the collaboration with the group of Prof. A. Meijerink at the Utrecht University. XRD and SEM results, which were presented in section 1.5, were also performed by this group. Although we received two samples with a concentration of 10% and 15% Er^{3+} , all measurements were carried out mainly with the former.

In the following, the experimental techniques and instrumentation that have been used during the development of this work are described. The spectroscopic techniques are: reflectance, excitation, luminescence, lifetime and Raman spectroscopy.

2.1 Diffuse reflectance

When working with microcrystalline powdered samples, it is not possible to obtain absorption or transmittance measurements directly (light must go through the sample) as in the case of a single crystal. Instead, reflectance spectra are obtained since they provide similar information about the transitions that take place between the ground state and excited states in the material. In fact, both magnitudes can be interrelated by using the so-called *Kramers-Krönig relations* (e.g. Fox, ref. [23]).

Diffuse reflectivity measurements at room temperature were performed by using a Cary 6000i (Varian) spectrophotometer, shown in Fig. 2.1(left). This system includes two different light sources and detectors, which allow measuring in a wavelength range from 170 to 1800 nm (UV-VIS-NIR). After the incidence of a light beam on the sample, the diffuse reflected light suffers multiple reflections in the inner surface of an integrating sphere (made of Teflon to make it fully reflective), and then reaches the detector (see Fig. 2.1(right)).

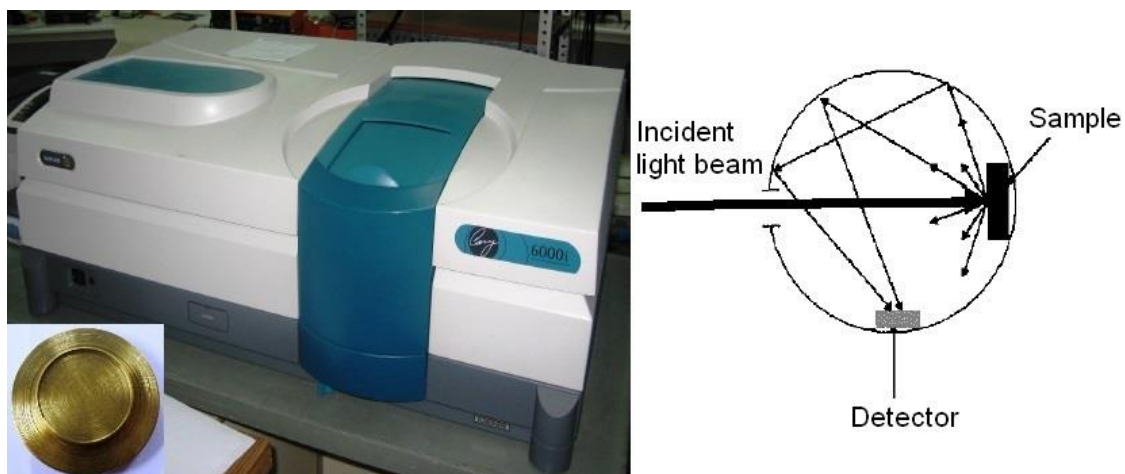


Figure 2.1: Left: Cary 6000i spectrophotometer and sample holder (inset). Right: schematic drawing of an integration sphere showing how it works. Ref. [24].

The procedure starts measuring the reflectance spectrum of a Teflon disc, that corresponds to the baseline. Afterwards, a small quantity of the material is placed and compacted on a sample holder and the same measurement is repeated for the sample. This is corrected taking into account the baseline. The result is automatically converted into an absorbance spectrum by the software. In summary, measuring the amount of light reflected at each wavelength it is possible to identify the excited energy levels of Er^{3+} ions in the $\text{Gd}_2\text{O}_2\text{S}$ lattice as peaks in the final spectrum.

2.2 Excitation and luminescence

In order to obtain an emission spectrum, the light intensity emitted by the material is measured at different wavelengths while the excitation wavelength of the light is fixed. On the other hand, an excitation spectrum requires detecting light at a fixed wavelength while the excitation wavelength or energy is scanned.

The spectrofluorimeter FLS920 from Edinburgh Instruments (shown in Fig. 2.2) was used to record both emission and excitation spectra. This system includes different light sources: a continuous and a pulsed xenon lamp, and a 980 nm laser diode. Before the incidence of the light beam on the sample, light is dispersed by a double monochromator (except in the case of the laser). This also occurs for the emitted light before it reaches the appropriate detector for the VIS or NIR range: a photomultiplier or an InGaAs array, respectively. For these measurements, the sample was seated in a capillary tube.

The efficiency of the detector and the power of the light source are both wavelength dependent. For this reason, it is imperative to correct the experimental spectrum taking into account the system response. So, we obtain the intrinsic emission of the sample. All spectra have been corrected for the system response.

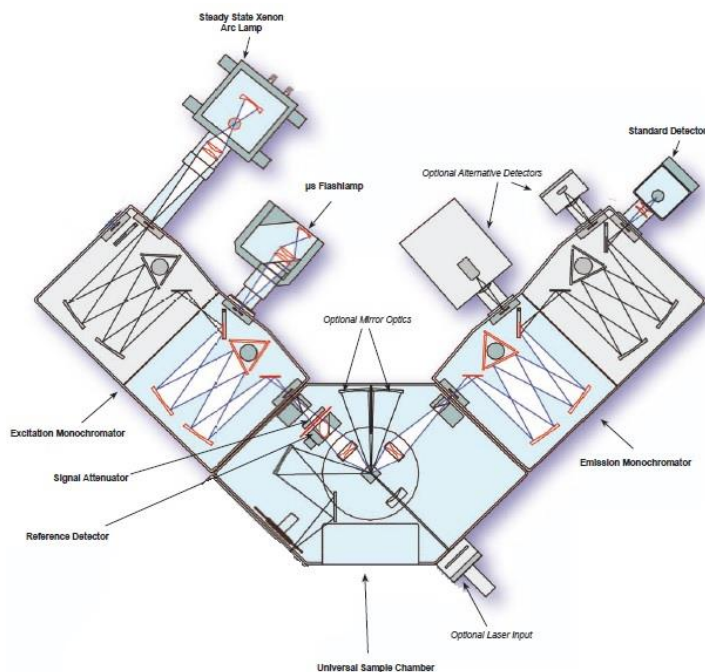


Figure 2.2: Spectrofluorimeter inner structure, showing several light sources and detectors.

An additional setup was used to obtain emission spectra (see Fig. 2.3). The light source consisted on a tunable OPO system (Opotek Vibrant B 355 II) pumped by the third harmonic of a Nd:YAG laser (Quantel). This allows pulsed excitation in a continuous range from 410 to 2400 nm, with a pulse width below 10 ns and a repetition rate of 10 Hz. The light emitted by the sample (in a capillary tube) is collected by a microscope objective at 90° with respect to the incident beam in order to avoid detecting light from the source. Then, light is transmitted through an optical fiber and it is dispersed by a monochromator (Triax320) before it reaches the detector. This device is an ICCD which works in a wavelength range between 180 and 850 nm.

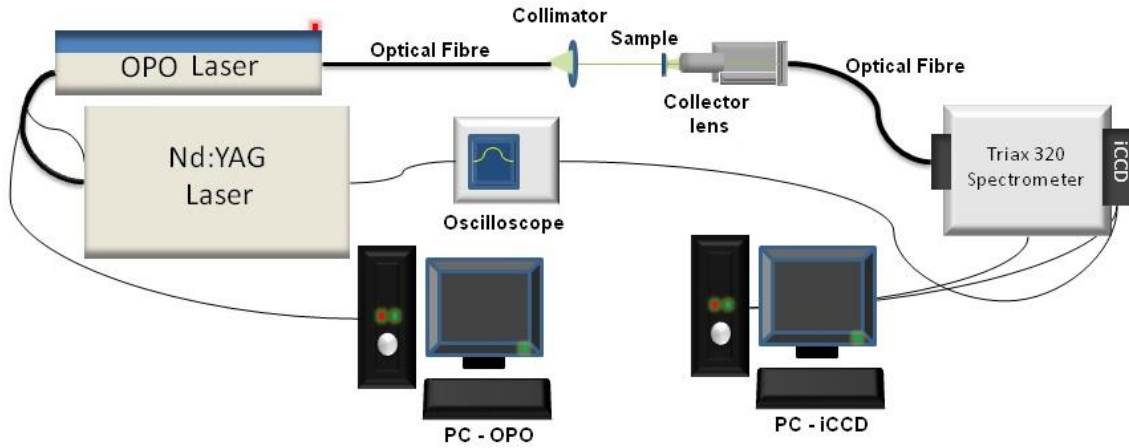


Figure 2.3: Scheme of the setup used to measure emission spectra after short-pulsed excitation.

This setup was also used with a 795 nm laser diode. It was pulsed using its driver in order to avoid the measurement of the intense light of the source.

According to *Stokes law* the emission spectrum is shifted to lower energies relative to the absorption/excitation spectrum, that energy difference is known as the Stokes shift. For this reason emission spectra are usually measured for energies lower than the excitation (in other words, larger wavelengths than the excitation radiation). However, due to up-conversion mechanisms it is possible to detect luminescence at higher energies (or shorter wavelengths) than that of the incident light. This is why this process is also called anti-Stokes luminescence.

2.3 Lifetime measurements

For the purpose of studying the temporal evolution of luminescence as a function of time, the emission intensity is measured with short-pulsed excitation. Lifetime is estimated by fitting the resulting data to a single or bi-exponential decay:

$$I(t) = Ae^{-t/\tau_1} \quad (13)$$

$$I(t) = Ae^{-t/\tau_1} + Be^{-t/\tau_2} \quad (14)$$

Or to a Vial's type equation [4] (only in case of UC):

$$I(t) = Ae^{-t/\tau_D} - Be^{-t/\tau_R} \quad (15)$$

where τ_D and τ_R represent the decay and rise time, respectively, which are expected for ETU.

Again, two different setups have been used to measure the lifetime of the emitting energy levels. The first one was the FLS920 spectrofluorimeter using the pulsed lamp (microseconds) and the laser as excitation sources.

On the other hand, the second setup consists on a photomultiplier (Hamamatsu R928) connected to a multichannel scaler (Stanford Research SR430), which records the detected signal (see Fig. 2.4). This system allows time-resolved photon counting measurements with a maximum temporal resolution of 5 ns.

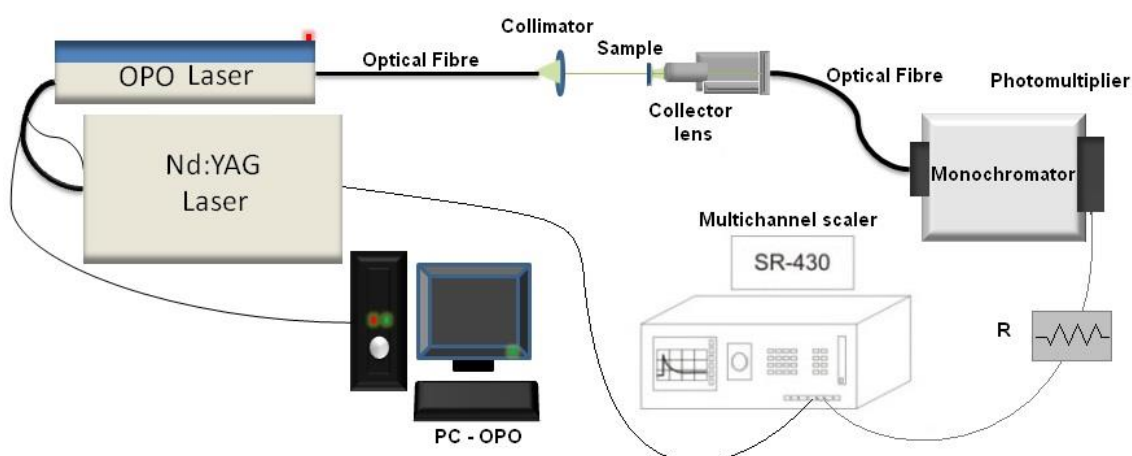


Figure 2.4: Scheme of the setup used to measure the temporal evolution of luminescence.

2.4 Low temperature measurements

Luminescence, excitation and lifetime measurements were performed as a function of T from 10 to 300 K using a closed-cycle helium cryostat in the FLS920 spectrofluorimeter. The material was placed in a copper sample holder and protected by a sapphire crystal.

The main advantage of low temperature spectra is that they may exhibit fine structure, which is unresolved at room temperature. This means that since hot bands are avoided, it is possible to determine the crystal-field splitting. The temperature dependence of the luminescence intensity and lifetime can be studied too.

Also, if the luminescent ion can be placed at different not-equivalent sites (with different local symmetry), this would have an effect on the excitation and emission spectra. However, this is not our case.

2.5 Raman

Raman spectroscopy studies the fraction of light that is scattered in an inelastic photon process. Contrary to Rayleigh scattering, the scattered photon energy differs from that of the incident photon: it is lower for Stokes lines and higher for anti-Stokes lines (see Fig. 2.5). In both cases lines are much weaker (about 3 orders of magnitude) than the main one, which corresponds to Rayleigh process. This energy difference is related to the characteristic phonon frequencies of the host material ($\hbar\omega$), so identification of Raman-active vibrational modes can be achieved through Raman spectroscopy.

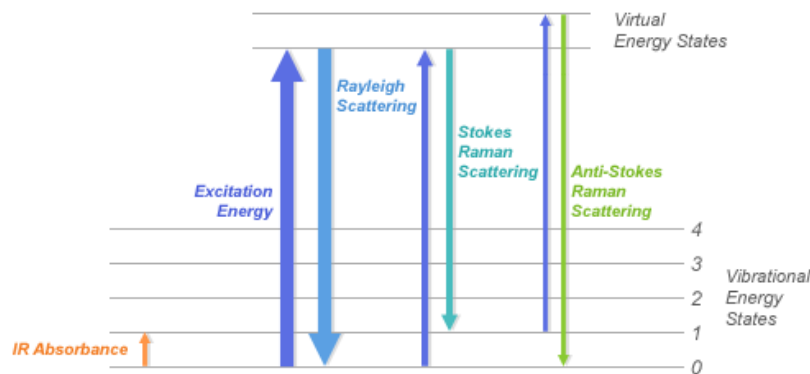


Figure 2.5: Energy level scheme for Raman effect, ref. [25]. For Raman spectroscopy, usually Stokes lines are detected since they are more intense than anti-Stokes lines.

Raman spectra were obtained using a triple spectrometer (Jobin-Yvon, T64000) which has a detection system that consists on three monochromators of 640 mm of focal length (for high resolution) and a N₂ cooled CCD detector. As light source, an Ar-Kr laser which allows working with several wavelengths was used. However, if the frequency of the incident beam is resonant with a transition to an excited electronic energy level, the Raman spectrum can be masked by fluorescence (since the latter is much more intense). This happens in our case for most of the excitation wavelengths of the Ar-Kr laser (514.5 nm, 647 nm, for example), and only exciting at 488 nm and 568 nm allows to observe Stokes lines.

3 RESULTS AND DISCUSSION

In this chapter, the most relevant results dealing with the optical properties of the material under study are presented. They were obtained through several experimental measurements, which were carried out along the development of this work.

A diffuse reflectance spectrum and a Raman spectrum were measured in order to study the host material, $\text{Gd}_2\text{O}_2\text{S}$, in which the optically active ion, Er^{3+} , has been incorporated. In addition to these, excitation and emission spectra were obtained in the NIR-VIS-UV range. The crystal-field splitting of the ground state as well as some emitting states have been obtained from the temperature dependence of these emission and excitation spectra. Additionally, up-conversion luminescence from multiple excitation wavelengths has been demonstrated for the first time for a single compound.

The temporal evolution of luminescence intensity was measured. Hence, we could determine the lifetime of the energy levels under different excitation energies and UC processes could be distinguished.

3.1 Dopant and host characterization

3.1.1 Erbium ions energy levels

The absorption spectrum shown in Fig. 3.1 was obtained from diffuse reflectance measurements performed at room temperature with a $\text{Gd}_2\text{O}_2\text{S}:\text{Er}^{3+}$ (15%) sample.

The experimental spectrum was compared with the Dieke diagram (see section 1.1.2) in order to assign the absorption peaks to the energy levels of Er^{3+} . The transitions took place between the ground state and the excited states, which are labeled in the figure. States with energy above approximately 37000 cm^{-1} are masked by the absorption edge of the host material.

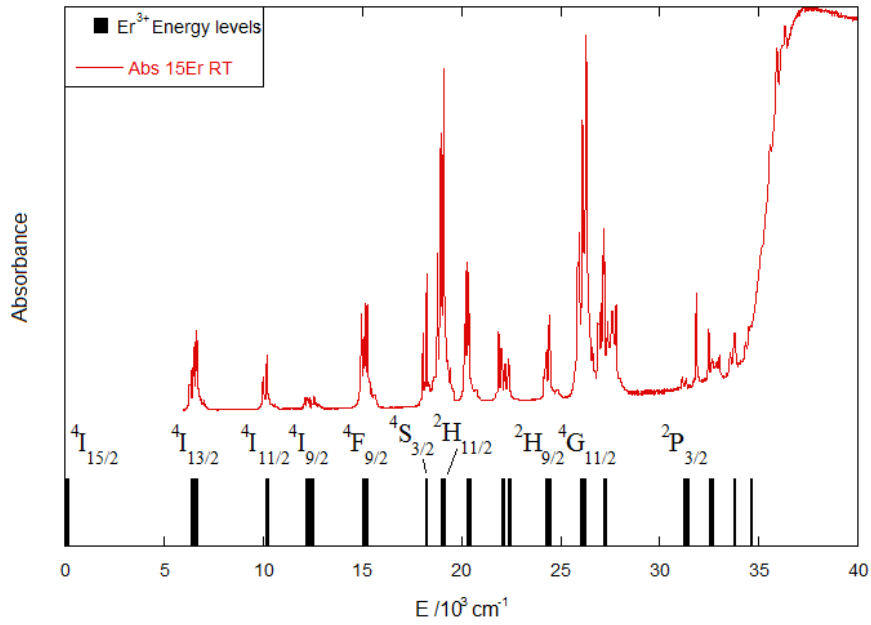


Figure 3.1: Absorption spectrum of $\text{Gd}_2\text{O}_2\text{S: Er}^{3+}$ (15%) and energy level diagram.

3.1.2 Raman spectrum

The Raman spectrum was measured with a $\text{Gd}_2\text{O}_2\text{S: Er}^{3+}$ (10%) sample at room temperature. Due to the extensive energy level structure of Er^{3+} ions, Raman scattering was masked by luminescence for some of the excitation laser wavelengths we tried (514.5 nm and 647 nm, for example). The one shown in Fig. 3.2 was obtained working with light of wavelength 488 nm, and coincident peaks were found for 568 nm excitation.

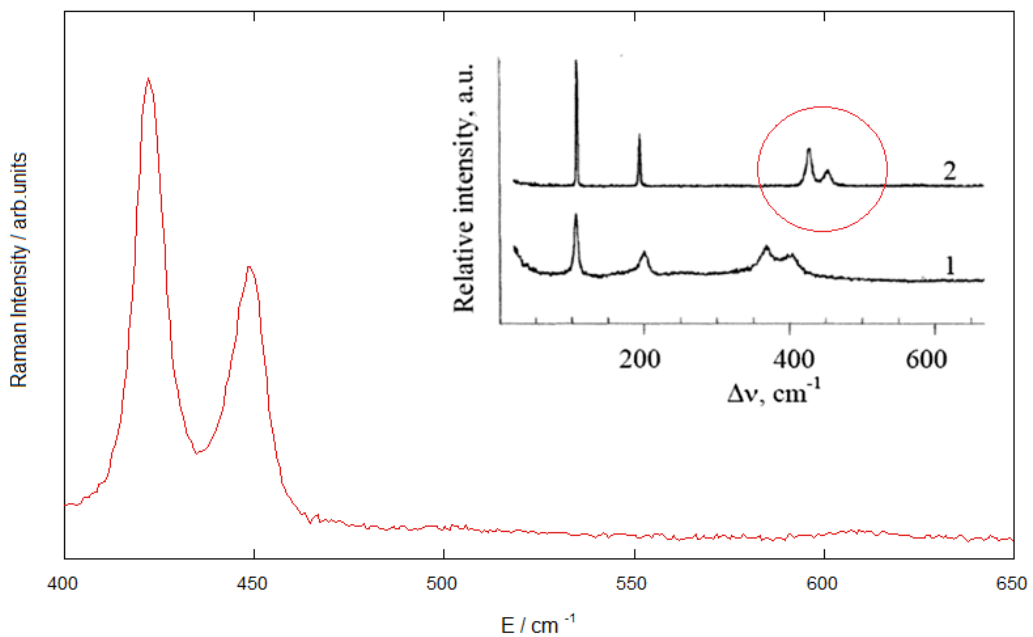


Figure 3.2: Raman spectrum of $\text{Gd}_2\text{O}_2\text{S: Er}^{3+}$ (10%). The inset (2) shows the Raman spectrum of $\text{Gd}_2\text{O}_2\text{S: Nd}^{3+}$ [26].

The resultant spectrum is compared in the figure with the Raman spectrum of $\text{Gd}_2\text{O}_2\text{S}$ doped with Nd^{3+} , from refs. [26, 27]. The measured peaks correspond to those inside the red circle, peaking at 428cm^{-1} and 452cm^{-1} . The value of the maximum phonon energy is around $\hbar\omega_{max} = 450\text{cm}^{-1}$, which is a characteristic of the host material. This energy agrees well with the known vibrational frequencies of the Gd-O bonds [28].

3.2 Excitation and emission of Er^{3+} -doped $\text{Gd}_2\text{O}_2\text{S}$

3.2.1 Excitation spectra

The excitation spectrum of $\text{Gd}_2\text{O}_2\text{S}:\text{Er}^{3+}(10\%)$ between 250 and 850 nm ($11750\text{-}40000\text{cm}^{-1}$) was obtained measuring the emitted light around 980 nm (10200cm^{-1}), which is due to an intense transition from the $^4I_{11/2}$ excited state to the $^4I_{15/2}$ ground state. Measurements were carried out from 10 K to 300 K every 50 K. However, only three of them are shown in Fig. 3.3 for the sake of clarity.

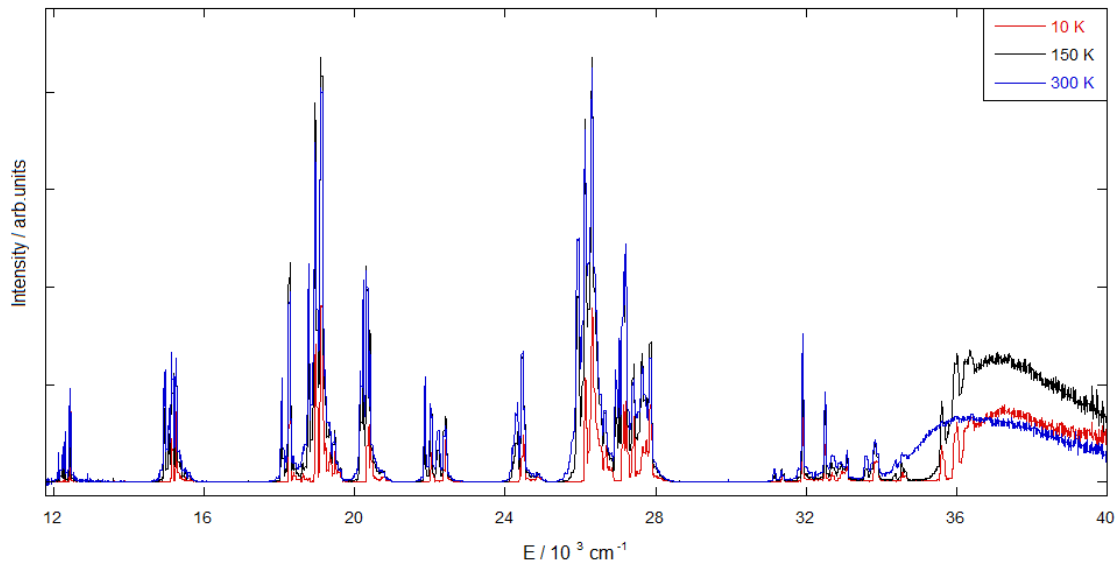


Figure 3.3: Excitation spectra of the $^4I_{11/2} \rightarrow ^4I_{15/2}$ emission at 980 nm for $\text{Gd}_2\text{O}_2\text{S}:\text{Er}^{3+}(10\%)$ measured at different temperatures. The broad band above 36000cm^{-1} is due to the absorption edge of the material.

The excitation peaks correspond to electronic transitions from the ground state to upper excited states. The excitation spectra are very similar to the absorbance spectrum. Both measurements have contributed to build the energy level diagram shown in Fig. 3.5 and also to know the appropriate wavelength at which Er^{3+} emission can be excited.

The temperature dependence of the high resolution excitation spectra will be used to study the crystal-field splitting of some states in section 3.2.3.

3.2.2 Temperature dependence of the emission intensity

Emission spectra of $\text{Gd}_2\text{O}_2\text{S: Er}^{3+}$ (10%) in the VIS-NIR range were obtained at different temperatures from 10 to 300 K. They were measured under high energy excitation (278 nm, 36000 cm^{-1}) and upon excitation into the $^4I_{11/2}$ level at 980 nm (10200 cm^{-1}).

The energy level diagram shown in Fig. 3.4, includes the energy states of the Er^{3+} ions and the host lattice levels (in grey), which are responsible for the interband transitions (absorption edge).

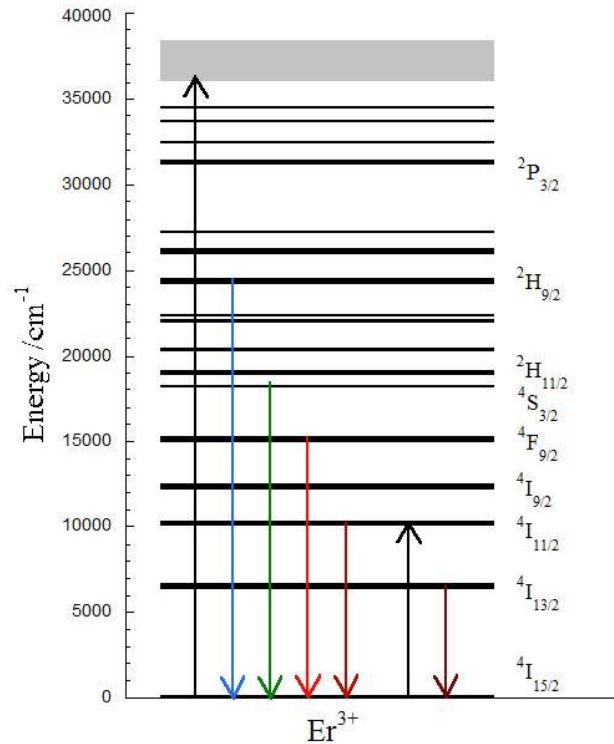


Figure 3.4: Energy level diagram of Er^{3+} ions. Black arrows show the excitation energies used, whereas the emissions for which the temperature dependence of the integrated intensity has been studied are shown by colored arrows. The thick grey lines over 36000 cm^{-1} represent the host lattice levels, the ones responsible for the great absorption over this energy.

A room temperature survey emission spectrum is shown in Fig. 3.5. Some intervals have been multiplied by a factor of 10 so that we can appreciate the weakest emission bands.

The most relevant and intense emission bands are found around 6300, 10000, 15000, 18000, and 24200 cm^{-1} . Hence, they correspond to electronic transitions from the $^2H_{9/2}$, $^2H_{11/2} - ^4S_{3/2}$, $^4F_{9/2}$, $^4I_{11/2}$ and $^4I_{13/2}$ excited states to the ground state ($^4I_{15/2}$), as it is drawn in Fig. 3.4. The other observed bands are due to inter-excited state transitions.

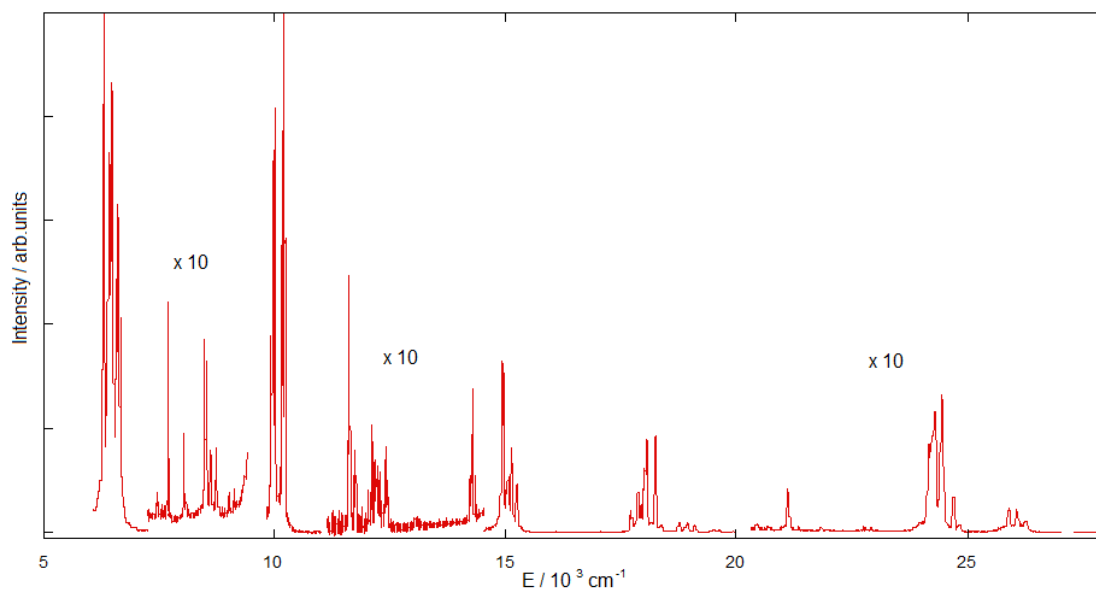


Figure 3.5: Room temperature survey emission spectra under excitation at 278 nm and 980 nm.

The red emission at 15000 cm^{-1} is approximately one third of the NIR emission observed at 10000 cm^{-1} . Moreover, while the maximum of the green emission (18000 cm^{-1}) is approximately one half of the red one, the blue emission (24200 cm^{-1}) is almost 10 times smaller.

The area under these bands has been integrated in order to investigate the evolution of the emission intensity with temperature. The results are shown in figures 3.6-3.10 of this section. Measurements were carried out from 10 K to 300 K every 50 K. The area has been calculated for each temperature, however, only some of the recorded spectra are shown for the sake of clarity.

Figure 3.6 shows the blue emission assigned to the ${}^2H_{9/2} \rightarrow {}^4I_{15/2}$ transition. The maximum intensity of this band is found at 75 K while at 300 K this value is 10 times smaller. This decrease is connected with the fact that the multi-phonon relaxation process is more efficient for higher temperatures, since phonon creation is more probable.

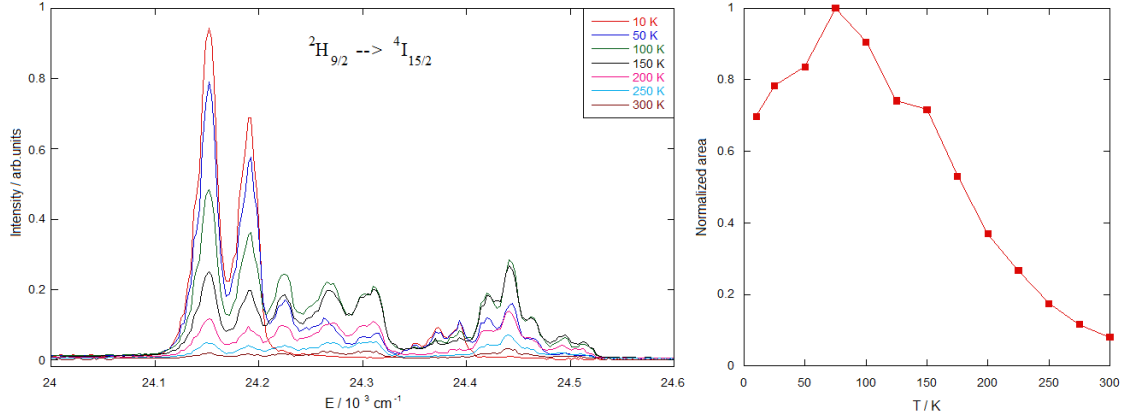


Figure 3.6: Left: ${}^2H_{9/2} \rightarrow {}^4I_{15/2}$ emission spectrum of $\text{Gd}_2\text{O}_2\text{S: Er}^{3+}(10\%)$ measured at different temperatures after 278 nm excitation. Right: Normalized temperature dependence of the integrated intensity of this emission. Lines are guides for the eye.

We should remember that there are various facts that can enhance or diminish luminescence from a specific state. On one hand, odd parity vibrational modes make intraconfigurational transitions through the ED mechanism possible. On the other, a non-radiative transition is more probable when more phonons are created. They are opposite contributions since both processes are temperature dependent. Phonon-assisted transitions or the temperature dependence of absorption cross-section must also be considered.

In Fig.3.7 the green emission corresponding to the ${}^4S_{3/2} \rightarrow {}^4I_{15/2}$ and ${}^2H_{11/2} \rightarrow {}^4I_{15/2}$ transitions is shown. The latter has been multiplied by a factor of 40 in the inset, since it is much less intense. The intensity emitted associated to the ${}^4S_{3/2} \rightarrow {}^4I_{15/2}$ transition (blue points) has a similar temperature dependence than that shown in the previous figure, although the maximum is reached at 100 K. On the other hand, the emission from ${}^2H_{11/2}$ (red points) increases with temperature. This happens because the energy difference, $\Delta E = E_2 - E_1$, is of the order of kT , so the population of both states, A_1 and A_2 , are related through the Boltzmann population factor:

$$\frac{A_2}{A_1} \propto \exp\left(-\frac{\Delta E}{kT}\right) \quad (16)$$

where k is the Boltzmann constant and T is the absolute temperature. Hence, the emission band of the level with higher energy grows as temperature increases. It is said that these energy levels are thermalized or thermally coupled.

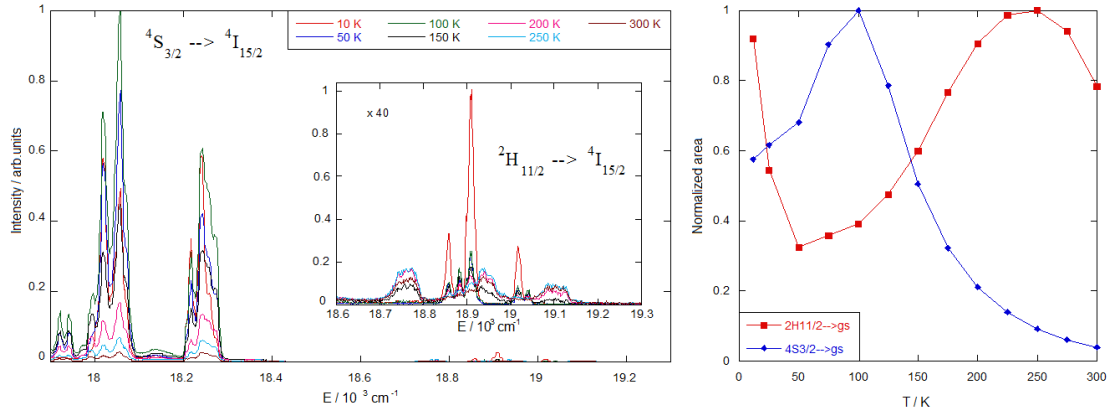


Figure 3.7: Left: $^4S_{3/2} \rightarrow ^4I_{15/2}$ and $^2H_{11/2} \rightarrow ^4I_{15/2}$ (inset) emission spectra of $\text{Gd}_2\text{O}_2\text{S: Er}^{3+}(10\%)$ measured at different temperatures after 278 nm excitation. Right: Normalized temperature dependence of the integrated intensity of these emissions. Lines are guides for the eye.

The ratio between the emission intensity from the $^2H_{11/2}$ and the $^4S_{3/2}$ state versus temperature has been plotted in Fig. 3.8. As it is shown, the result can be fitted to an exponential curve, which confirms that the population of both energy levels is thermally coupled. Also, we can conclude from the fitting parameters that the energy difference between these states is around $700 \pm 30 \text{ cm}^{-1}$, which agrees with the energy difference between Stark levels of $^2H_{11/2}$ and $^4S_{3/2}$ in Fig. 3.7.

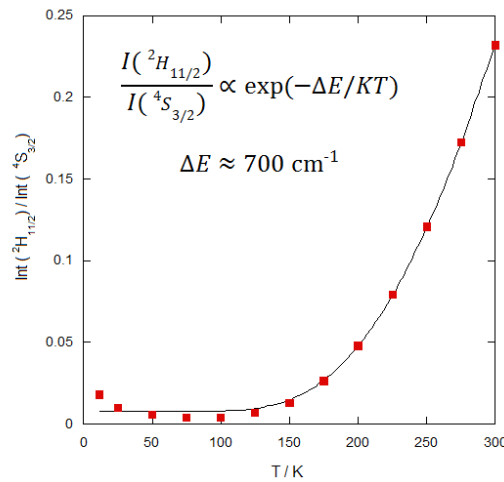


Figure 3.8: ratio between the intensity emitted due to the $^2H_{11/2} \rightarrow ^4I_{15/2}$ transition and the $^4S_{3/2} \rightarrow ^4I_{15/2}$ transition versus temperature. The black line is the result of a fitting procedure according with the equation shown.

Figure 3.9 shows the temperature dependence of the red emission associated to the ${}^4F_{9/2} \rightarrow {}^4I_{15/2}$ transition. The intensity of this band decreases almost continuously: the maximum is found at 10 K and there is a local maximum at 75 K.

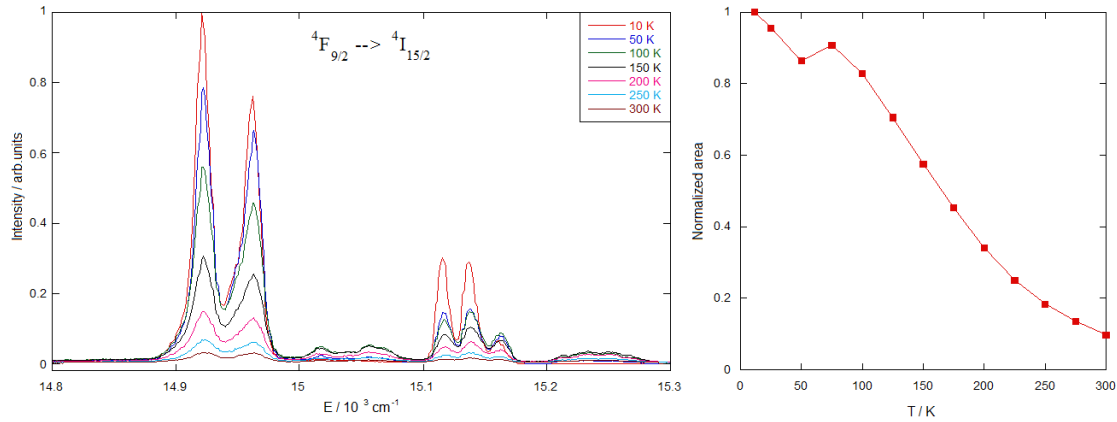


Figure 3.9: Left: ${}^4F_{9/2} \rightarrow {}^4I_{15/2}$ emission spectrum of $\text{Gd}_2\text{O}_2\text{S: Er}^{3+}(10\%)$ measured at different temperatures after 278 nm excitation. Right: Normalized temperature dependence of the integrated intensity of this emission. Lines are guides for the eye.

We have tried to fit the temperature dependence of this emission intensity to an Arrhenius-type law for multi-phonon relaxation:

$$I = \frac{I_0}{1 + b \exp(-\Delta E / kT)} \quad (17)$$

where I_0 is the intensity emitted at $T = 0$ and b is connected with the degeneracy of the states involved in the transition.

This equation implies that there is an activation energy, ΔE , over which de-excitation through multi-phonon relaxation processes starts to compete with luminescence, so the latter decreases with temperature. As a result of the fitting process we obtained an activation energy around 300 cm^{-1} .

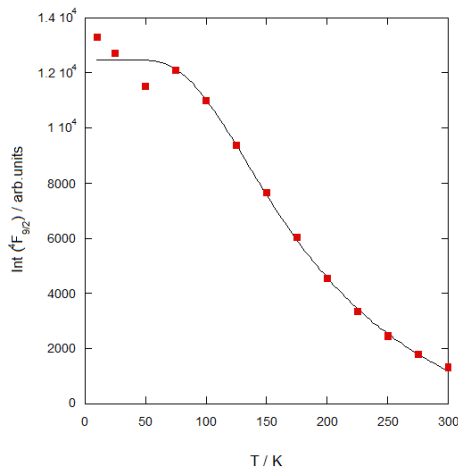


Figure 3.10: intensity emitted due to the ${}^4F_{9/2} \rightarrow {}^4I_{15/2}$ transition versus temperature. The black line is the result of a fitting procedure to eq. (17).

Figure 3.11 shows the near-infrared emission of the ${}^4I_{11/2} \rightarrow {}^4I_{15/2}$ transition. This emission band grows with temperature until 175 K is reached. Then, at 300 K, the area is approximately one third of the maximum value.

The gap to the ${}^4I_{13/2}$ next lower level is about 3500 cm^{-1} , which corresponds to a minimum of 8 phonons in this material. This makes losses due to multi-phonon relaxation negligible [4]. However, as it is shown in Fig.3.12, when exciting into the ${}^4I_{11/2}$ level, emission from ${}^4I_{13/2}$ increases with temperature. This may be connected with cross relaxation processes enhanced by temperature.

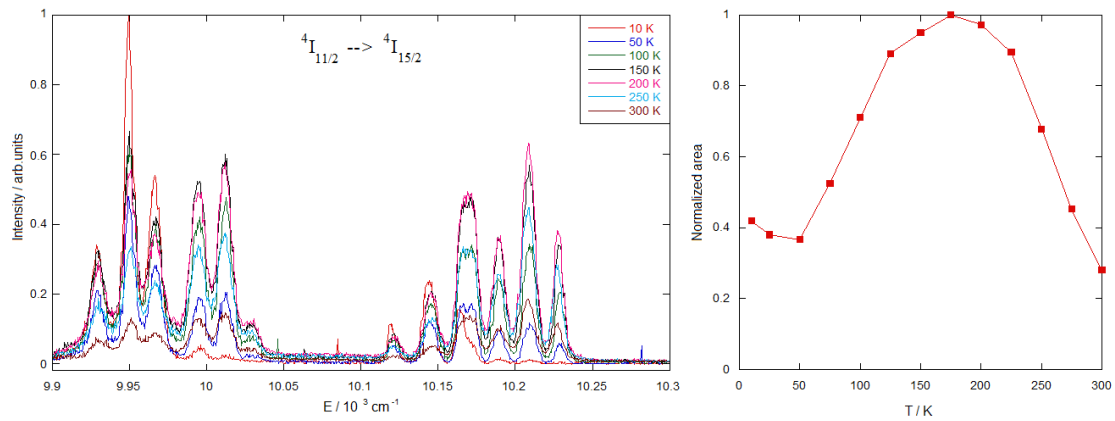


Figure 3.11: Left: ${}^4I_{11/2} \rightarrow {}^4I_{15/2}$ emission spectrum of $\text{Gd}_2\text{O}_2\text{S:Er}^{3+}(10\%)$ measured at different temperatures after 278 nm excitation. Right: Normalized temperature dependence of the integrated intensity of this emission. Lines are guides for the eye.

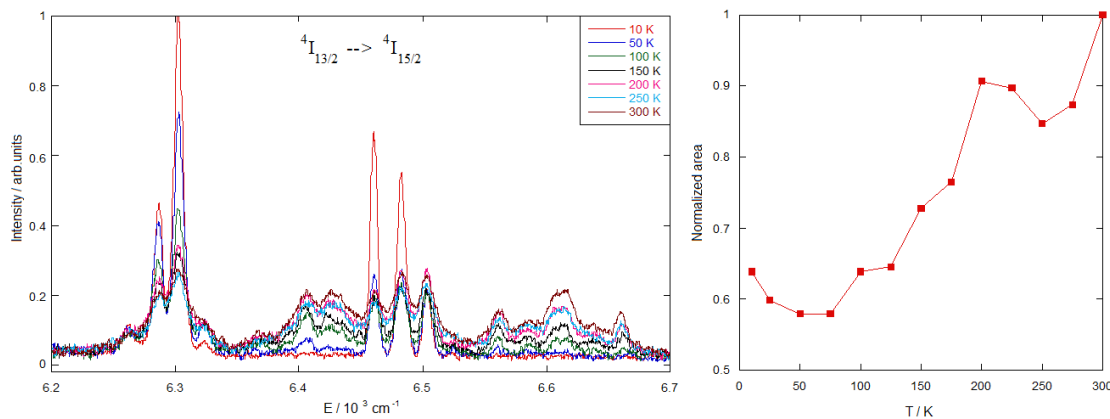


Figure 3.12: Left: ${}^4I_{13/2} \rightarrow {}^4I_{15/2}$ emission spectrum of $\text{Gd}_2\text{O}_2\text{S:Er}^{3+}(10\%)$ measured at different temperatures after 980 nm excitation. Right: Normalized temperature dependence of the integrated intensity of this emission. Lines are guides for the eye.

3.2.3 Splitting of ${}^4I_{15/2}$ (g.s.), ${}^4F_{9/2}$, and ${}^4S_{3/2}$ states - Stark levels

It is possible to distinguish fine structure in low temperature spectra, and thus investigate the energy level splitting due to the crystal field interaction. In this work, Stark sublevels of the ground state were observed in emission spectra from the ${}^4F_{9/2}$ and ${}^4S_{3/2}$ states.

We assume that at 10 K emission takes place from the lowest Stark level of these states, so that the peaks in Fig.3.13 correspond to transitions to the Stark sublevels of the ${}^4I_{15/2}$ state (g.s.). According to *Kramers' theorem* (see section 1.1.2), the maximum number of components in which the ground state of the Er^{3+} ion can split is 8, but only 5 are observed. The relative positions of the peaks in both plots (see group of lines) were compared in order to reach an agreement and to determine the energy of the ground state Stark sublevels. In comparison with the lowest one, ${}^4I_{15/2}$ (0, 1, 2, 3, 4) levels have energies: 0, 22, 45, 202, and 240 cm^{-1} .

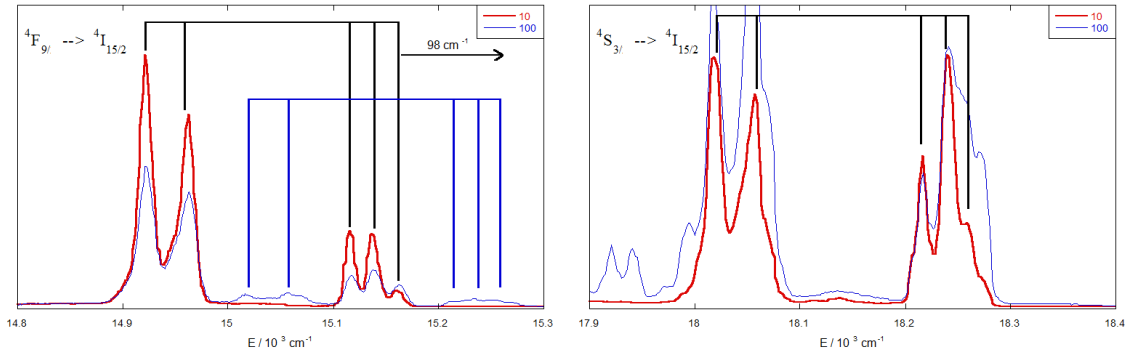


Figure 3.13: ${}^4F_{9/2} \rightarrow {}^4I_{15/2}$ (left) and ${}^4S_{3/2} \rightarrow {}^4I_{15/2}$ (right) emission spectra of $\text{Gd}_2\text{O}_2\text{S: Er}^{3+}$ (10%) measured at 10 and 100 K after 278 nm excitation. Black lines indicate transitions from the lowest Stark sublevel of these states to the components (0, 1, 2, 3, 4) in which the ${}^4I_{15/2}$ state (g.s.) splits. Blue lines (left) are shifted 98 cm^{-1} to higher energies.

At higher temperatures, like 100 K, additional peaks are found for the ${}^4F_{9/2} \rightarrow {}^4I_{15/2}$ red transition (Fig.3.13, left) while the “original” peaks become less intense. These new peaks are shifted to higher energies by 98 cm^{-1} . The reason is that the next Stark sublevel of the ${}^4F_{9/2}$ state is populated, so more energetic emissions take place.

On the other hand, the ${}^4S_{3/2} \rightarrow {}^4I_{15/2}$ emission (Fig.3.13, right) does not show any shifted peaks. In theory, this level can only split in two components (since $J = 3/2$). However, in this case it stays degenerated or sublevels are close enough that they could not be resolved.

The Stark sublevels of the ${}^4F_{9/2}$ state were observed in the excitation spectrum (plotted in Fig.3.14). Five different sublevels were found, that is the maximum number of components in which this level can split. The result is that ${}^4F_{9/2}$ ($0'$, $1'$, $2'$, $3'$, $4'$) levels have energies: 15160, 15262, 15382, 15508, and 15613 cm^{-1} . Note that the energy difference between the $0'$ and $1'$ sublevels is 102 cm^{-1} , which almost matches the energy shift that explained the emission peaks that grow with temperature in Fig.3.13(left).

When temperature is increased, all the Stark sublevels of the ground state are populated. As a consequence, excitation occurs from 5 different electronic origins and peaks are shifted to lower energies. This shift perfectly matches the splitting of the ${}^4I_{15/2}$ state (shown in grey).

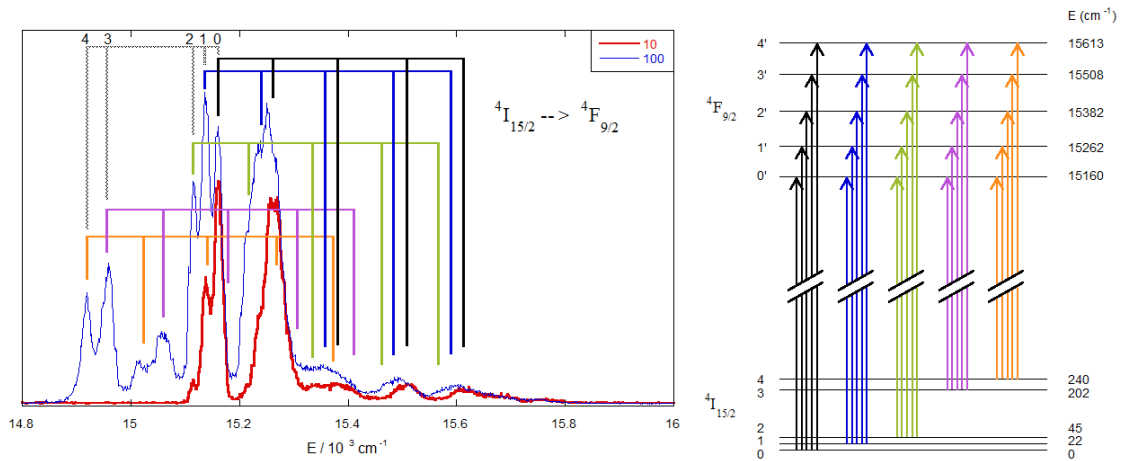


Figure 3.14: Left: ${}^4I_{15/2} \rightarrow {}^4F_{9/2}$ excitation spectrum of $\text{Gd}_2\text{O}_2\text{S: Er}^{3+}(10\%)$ measured at 10 and 100 K detecting at 980 nm. Each group of lines indicates transitions from one of the Stark sublevels ${}^4I_{15/2}$ (0, 1, 2, 3, 4) in black, blue, green, purple and orange, respectively. The grey lines indicate the energy splitting of the ${}^4I_{15/2}$ state, which coincides with the energy shift. Right: Energy level diagram showing the Stark sublevels of the ${}^4F_{9/2}$ and ${}^4I_{15/2}$ states, and the transitions responsible of the excitation spectrum (using the same color code).

In Fig. 3.14(right) a diagram with the Stark sublevels of the ${}^4F_{9/2}$ and ${}^4I_{15/2}$ states is shown. The splitting is of $\Delta E = 240 \text{ cm}^{-1}$ for the ground state and of $\Delta E = 453 \text{ cm}^{-1}$ for the excited state. The energy difference between their sublevels has been drawn at the same scale while the separation between states has not. The transitions responsible of the excitation spectrum are also shown.

In the ${}^4S_{3/2}$ excitation spectrum shown in Fig.3.15 no energy splitting of this state is observed, which coincides with the previous results. The peaks that appear at higher temperatures correspond to transitions from ${}^4I_{15/2}$ (0, 1, 2, 3, 4) sublevels to the ${}^4S_{3/2}$ state. Then, there is only one peak, which is shifted according with the splitting of the ${}^4I_{15/2}$ state (shown in grey).

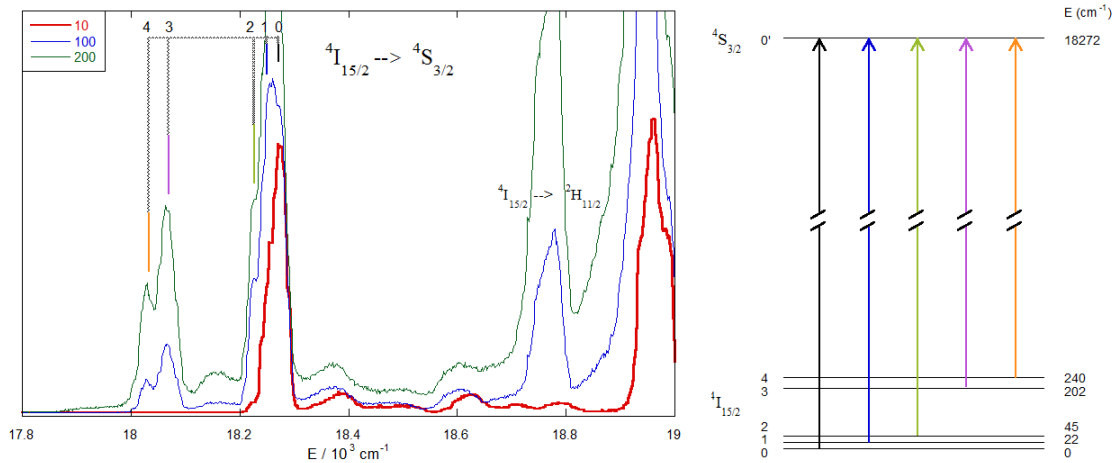


Figure 3.15: Left: ${}^4I_{15/2} \rightarrow {}^4S_{3/2}$ excitation spectrum of $\text{Gd}_2\text{O}_2\text{S: Er}^{3+}(10\%)$ measured at 10, 100 and 200 K detecting at 980 nm. Each color line indicates a transition from one of the Stark sublevels ${}^4I_{15/2}$ (0, 1, 2, 3, 4) in black, blue, green, purple and orange, respectively, to the ${}^4S_{3/2}$ state. The grey lines indicate the energy splitting of the ${}^4I_{15/2}$ state, which coincides with the energy shift of the observed peak. Right: Energy level diagram showing the Stark sublevels of the ${}^4S_{3/2}$ and ${}^4I_{15/2}$ states, and the transitions responsible of the excitation spectrum (using the same color code).

The fact that only five crystal-field components of the ground state, ${}^4I_{15/2}$, could be identified and that the ${}^4S_{3/2}$ excited state shows no splitting at all indicates that the symmetry of the lattice is relatively high. Otherwise, the states would split in as much components as possible according to their degeneracy (see section 1.1.2).

3.3 Up-conversion luminescence

3.3.1 Temperature dependence

Up-conversion emission spectra of $\text{Gd}_2\text{O}_2\text{S:Er}^{3+}(10\%)$ in the VIS range were obtained at different temperatures from 10 to 300 K. They were measured upon CW excitation into the ${}^4I_{11/2}$ level at 980 nm (10200 cm^{-1}).

A survey up-conversion luminescence spectrum measured at 300 K is shown in Fig. 3.16 (inset). NIR to VIS UC was achieved, and green and red luminescence associated to electronic transitions from the ${}^2H_{11/2} - {}^4S_{3/2}$ (18000 cm^{-1}) and ${}^4F_{9/2}$ (15000 cm^{-1}) excited states to the ground state (${}^4I_{15/2}$) were observed after excitation at around $1\mu\text{m}$.

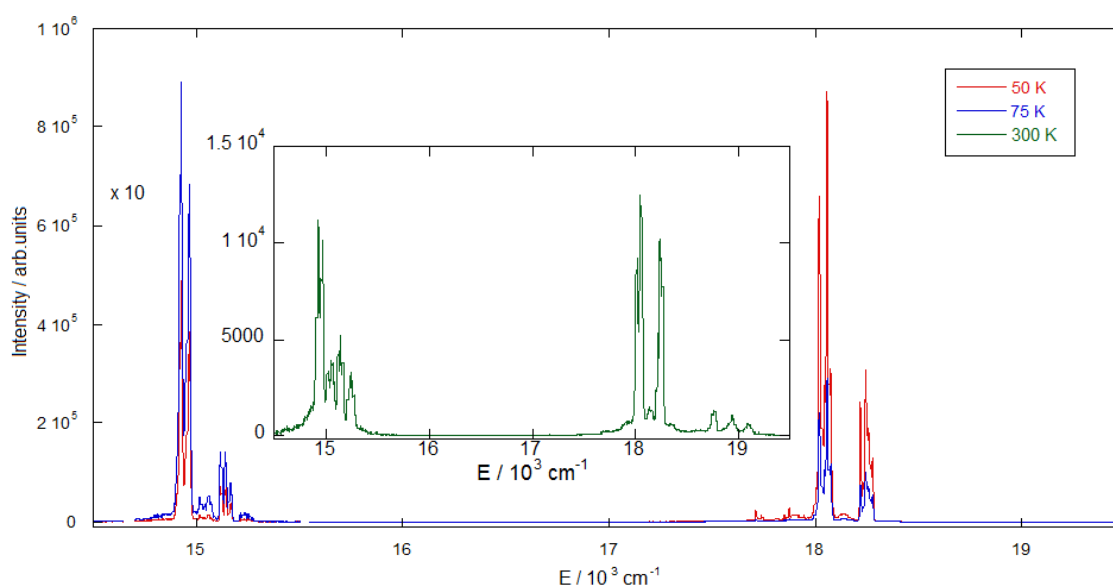


Figure 3.16: Emission spectra under excitation at 980 nm measured at 50 K and 75 K. The red band around (15000 cm^{-1}) has been multiplied by a factor of 10. The inset shows a survey UC emission spectrum upon 980 nm excitation measured at 300 K.

Emission at different temperatures is shown in figures 3.17 and 3.18, together with the temperature dependence of the emission intensity. Measurements were carried out from 10 K to 300 K every 50 K. The area has been obtained for each temperature, however, only some of the recorded spectra are shown for the sake of clarity.

Figure 3.17 shows the intensity emitted due to the ${}^2H_{11/2} \rightarrow {}^4I_{15/2}$ transition (red points), which increases with temperature. It is important to note that the ${}^2H_{11/2}$ band has been multiplied by a factor of 650. This value is more than 15 times greater for emission after an UC process than after excitation over the emitting level (see Fig.3.7).

However, the emission from ${}^4S_{3/2}$ (blue points) grows with temperature and then decreases, stabilizing for T over 150 K. This means that the dominant green UC emission has a similar temperature behavior than that observed in Fig.3.7 for normal emission, although the maximum has shifted to 50 K.

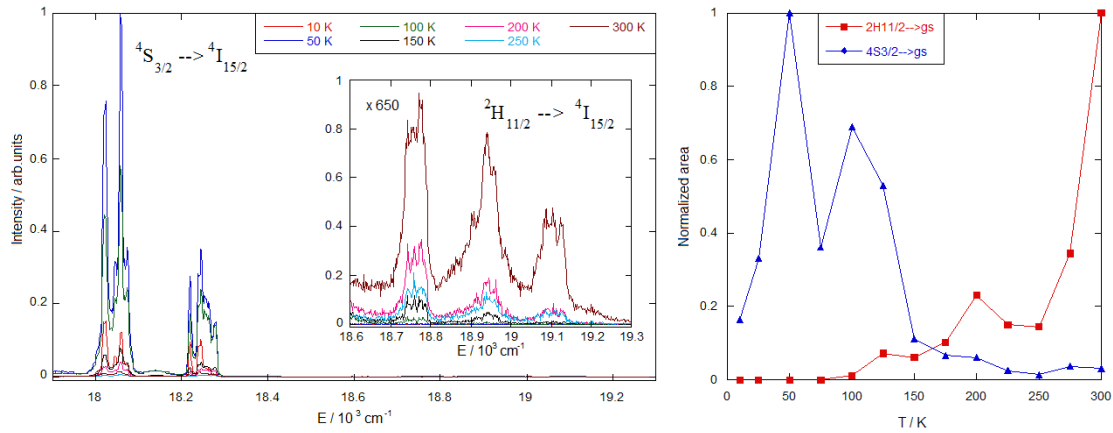


Figure 3.17: Left: ${}^4S_{3/2} \rightarrow {}^4I_{15/2}$ and ${}^2H_{11/2} \rightarrow {}^4I_{15/2}$ (inset) UC emission spectra of $Gd_2O_2S:Er^{3+}(10\%)$ measured at different temperatures after 980 nm excitation. Right: Normalized temperature dependence of the integrated intensity of this emission. Lines are guides for the eye.

Figure 3.18 shows the red emission corresponding to the ${}^4F_{9/2} \rightarrow {}^4I_{15/2}$ transition. While for normal luminescence emission only decreased (Fig. 3.9), now the strongest emission is found at 75 K. Then, for T over 150 K, intensity oscillates but keeps under half of this value. Multi-phonon relaxation, energy transfer processes and ETU up-conversion, all of which are temperature dependent, contribute to this behavior.

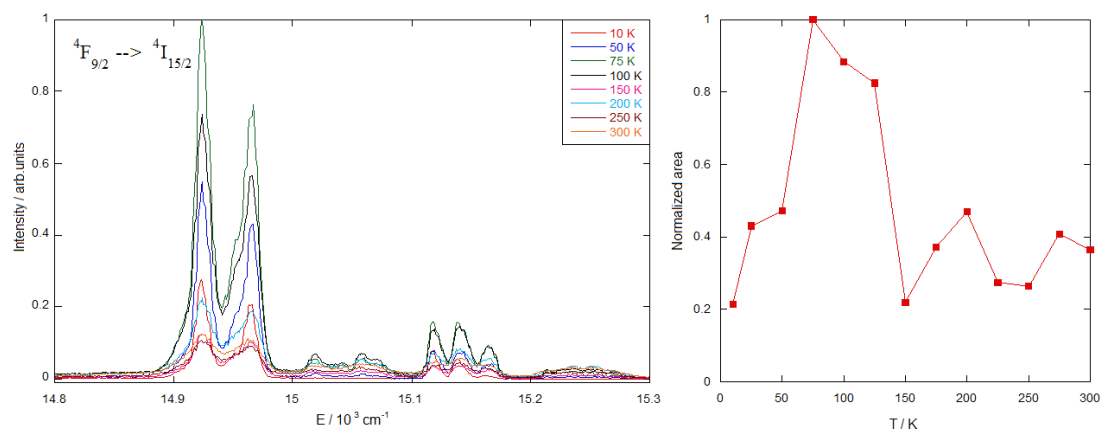


Figure 3.18: Left: ${}^4F_{9/2} \rightarrow {}^4I_{15/2}$ UC emission spectrum of $Gd_2O_2S:Er^{3+}(10\%)$ measured at different temperature, after 980 nm excitation. Right: Normalized temperature dependence of the integrated intensity of this emission. Lines are guides for the eye.

Since UC is very efficient in this material, during experimental measurements luminescence could be seen with the naked eye. Under IR excitation at room temperature (RT), a mixture of green and red light was observed.



Figure 3.19: Up-conversion luminescence of the $\text{Gd}_2\text{O}_3\text{:10\%Er}^{3+}$ sample upon 980 nm excitation at room temperature.

The green and red bands can be compared since they were measured under the exact same conditions. In fact, the region presented in the previous figures has been selected among one spectrum recorded between 500 and 850 nm ($11750\text{-}20000\text{ cm}^{-1}$) which was corrected for the system response. It is found that the maximum intensity emitted from ${}^4\text{S}_{3/2}$ (at 50 K) is approximately one order of magnitude bigger than the highest emission of ${}^4\text{F}_{9/2}$ (at 75 K) (see Fig. 3.17). However, at 300 K the former decreases so much that both bands even, although the green band keeps being the strongest (see Fig. 3.17(inset)). Since the human eye is more sensitive to yellowish-green light, the green emission “seems” to dominate. This is the case shown in Fig. 3.19.

On the other hand, if we consider normal emission (exciting at 278 nm) at 300 K, the intensity of the red band is almost twice that of the green band. This explains why with UV excitation it “seems” that more red light is observed.

3.3.2 Multi up-conversion

Up-conversion emission spectra of $\text{Gd}_2\text{O}_3\text{:Er}^{3+}(10\%)$ were recorded at room temperature upon excitation into different multiplets, so we induced UC luminescence exciting into the ${}^4\text{I}_{13/2}$, ${}^4\text{I}_{11/2}$, ${}^4\text{I}_{9/2}$, ${}^4\text{F}_{9/2}$ and ${}^4\text{S}_{3/2} - {}^2\text{H}_{11/2}$ levels (Fig. 3.20). Three UC emissions (blue, green and red) could be observed, which correspond to transitions from the ${}^2\text{H}_{9/2}$, ${}^4\text{S}_{3/2} - {}^2\text{H}_{11/2}$ and ${}^4\text{F}_{9/2}$ excited states to the ground state, respectively.

In contrast to the spectra presented in section 3.3.1, all the spectra shown in this section have been measured after short-pulsed excitation. The setup used corresponds to Fig. 2.3. Due to a greater excitation power, a more intense UC blue emission at room temperature was achieved.

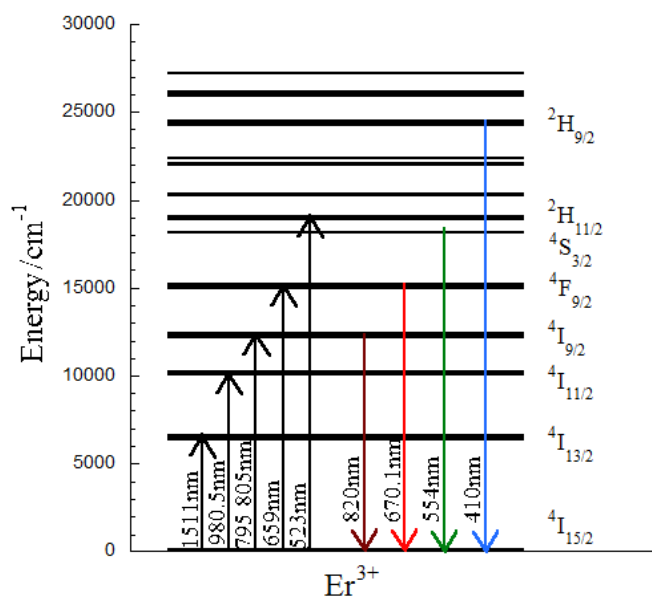


Figure 3.20: Energy level diagram of Er^{3+} ions. Arrows show the excitation and emission of NIR and VIS light. The wavelength indicated for each transition corresponds to that used in section 3.4 for lifetime measurements.

The energy level diagram of Er^{3+} ions in Fig. 3.20 shows the transitions responsible for the spectra presented in Fig. 3.21. However, the infrared emission from ${}^4I_{9/2}$ was not recorded, since it required another detector. Also, the excitation and emission wavelengths in this figure are those used for lifetime measurements in section 3.4. The excitation energy was slightly tuned in order to maximize the emission bands.

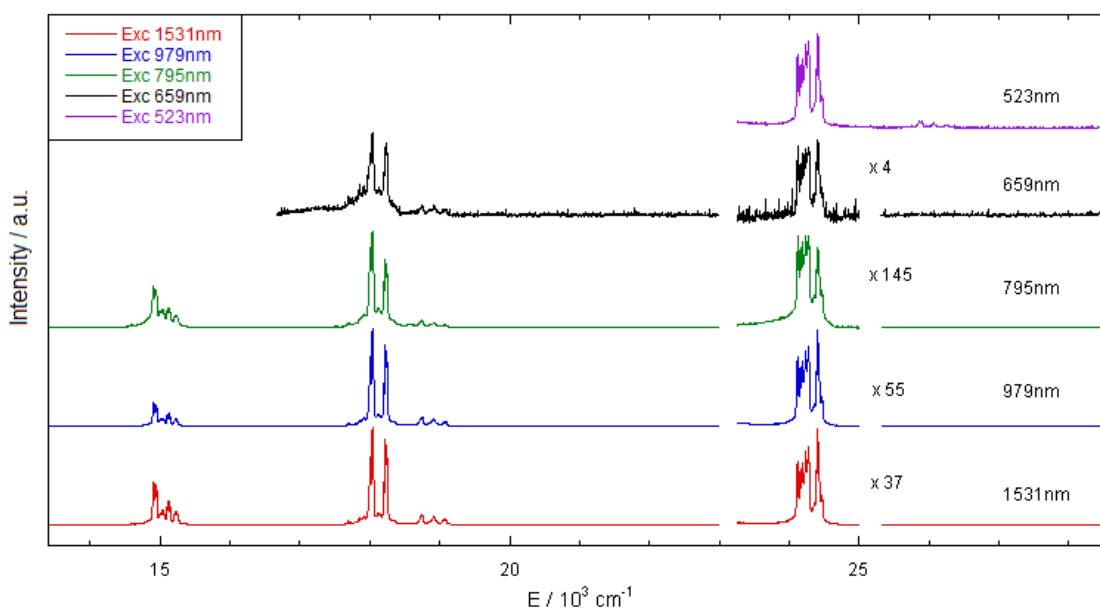


Figure 3.21: Up-conversion emission spectra, exciting at 523 nm(19100 cm^{-1}), 659 nm(15200 cm^{-1}), at 795 nm(12600 cm^{-1}), 979 nm(10200 cm^{-1}), and 1531 nm(6530 cm^{-1}).

Exciting at 523 nm (19100 cm^{-1}) a blue band corresponding to the ${}^2H_{9/2} \rightarrow {}^4I_{15/2}$ transition was observed. Although the ${}^2P_{3/2} \rightarrow {}^4I_{13/2}$ transition also gives rise to blue emission, it is much less intense (one order of magnitude). To obtain this blue emission at least 2 photons are needed.

Then, exciting at 659 nm (15200 cm^{-1}) allowed the observation of the band around 18000 cm^{-1} , which is associated to the ${}^4S_{3/2} \rightarrow {}^4I_{15/2}$ transition. At a slightly higher energy, the ${}^2H_{11/2} \rightarrow {}^4I_{15/2}$ transition is observed. Together both bands give rise to green emission. In this case, the population of the ${}^2H_{9/2}$ and ${}^4S_{3/2} - {}^2H_{11/2}$ excited states also involves a minimum of 2 photons.

Finally, excitation in the NIR region at 795 nm (12600 cm^{-1}), 979 nm (10200 cm^{-1}), and 1531 nm (6530 cm^{-1}) gives rise to three VIS bands: a red, a green and a blue one. The former corresponds to the ${}^4F_{9/2} \rightarrow {}^4I_{15/2}$ transition. For these excitation energies, the blue emission was also recorded independently so that the fine structure could be appreciated. In relation with the rest of the spectra, this band was multiplied by the factor shown in the figure. The distinct blue emission intensity can be correlated with the absorption cross section of the excited states involved in the up-conversion processes.

To obtain the blue emission associated to the ${}^2H_{9/2} \rightarrow {}^4I_{15/2}$ transition at least 2 photons are needed when exciting into the ${}^4I_{9/2}$ excited state since the energy of the emitting level is almost twice the excitation energy. On the other hand, excitation into the ${}^4I_{11/2}$ and ${}^4I_{13/2}$ states requires a minimum of 3 and 4 photons respectively to reach the ${}^2H_{9/2}$ state.

The population of the ${}^4S_{3/2} - {}^2H_{11/2}$ excited state involves a minimum of 2 photons under excitation into the ${}^4I_{9/2}$ and ${}^4I_{11/2}$ states. In fact, this level is reached after multiphonon relaxation from the next higher levels. Although excitation into the ${}^4I_{13/2}$ state requires 3 photons to achieve green emission, it has been demonstrated by power dependence experiments that an ETU process involving 4 photons is the main mechanism responsible for the population of this state. [4]

Red emission from the ${}^4F_{9/2}$ excited state to the ground state needs 2 photons when exciting into the ${}^4I_{9/2}$ and ${}^4I_{11/2}$ states and 3 photons for excitation into the first excited state, ${}^4I_{13/2}$.

Note that the blue band was not shown in the UC emission spectra presented in section 3.3.1. However, it was weakly observed at 10 K upon excitation at 278 nm. The setup used to obtain the results presented above offers a much higher power excitation. This may explain why the blue band can be properly recorded at room temperature. The importance of observing UC blue emission under excitation into 5 different energy levels should be stressed.

3.4 Lifetime of the erbium energy levels

The temporal evolution of the normal and UC luminescence intensity from different excited states, ${}^4I_{9/2}$, ${}^4F_{9/2}$, ${}^4S_{3/2} - {}^2H_{11/2}$ and ${}^2H_{9/2}$ in $\text{Gd}_2\text{O}_3\text{:Er}^{3+}(10\%)$ upon ns pulsed excitation into the ${}^4I_{13/2}$, ${}^4I_{11/2}$, ${}^4I_{9/2}$, ${}^4F_{9/2}$ and ${}^4S_{3/2} - {}^2H_{11/2}$ levels (see Fig. 3.20) was measured. Hence, the normal and UC lifetime of each state has been determined for different excitation energies (see figures 3.22 to 3.25 in this section).

The lifetime of a particular state under direct excitation measured for 10% Er^{3+} is usually shorter than for very low doping concentrations (intrinsic lifetime, τ_0) since non-radiative processes, such as multi-phonon relaxation, migration and up-conversion, take place.

The lifetime of the ${}^4I_{13/2}$, ${}^4I_{11/2}$, ${}^4I_{9/2}$, ${}^4F_{9/2}$, ${}^4S_{3/2} - {}^2H_{11/2}$ Er^{3+} excited states in $\text{Gd}_2\text{O}_3\text{:Er}^{3+}(0.1\%)$ measured by [4] are shown in Table 1, and will be used in our analysis.

Emitting state	$\tau_0(\text{Gd}_2\text{O}_3\text{:0.1\% Er}^{3+})$
${}^4I_{13/2}$	3.7 ± 0.1 ms
${}^4I_{11/2}$	2.30 ± 0.05 ms
${}^4I_{9/2}$	17.5 ± 0.5 μs
${}^4F_{9/2}$	100 ± 1 μs
${}^4S_{3/2} - {}^2H_{11/2}$	560 ± 20 μs

Table 1: Lifetimes of Er^{3+} excited states in $\text{Gd}_2\text{O}_3\text{:Er}^{3+}(0.1\%)$ measured by [4] after direct excitation in the emitting level.

The emission at 820 nm from the ${}^4I_{9/2}$ level under direct excitation at 805 nm shows a two exponential decay behavior ($\tau_1 = 0.87 \pm 0.02$ μs , $\tau_2 = 5.10 \pm 0.10$ μs) (Fig. 3.22(a)). This lifetime is much shorter than $\tau_0 = 17.5 \pm 0.5$ μs (Table 1). This behavior points to an important contribution of the non-radiative processes to de-populate this state.

Upon excitation into the next lower level, ${}^4I_{11/2}$, at 980.5 nm (Fig. 3.22(b)), a single exponential decay ($\tau = 725 \pm 9$ μs) is observed. Finally, excitation into the first excited state, ${}^4I_{13/2}$, at 1511 nm (Fig. 3.22(c)) gives rise to a bi-exponential decay ($\tau_1 = 206 \pm 4$ μs , $\tau_2 = 1.138 \pm 0.017$ ms).

In both cases, the presence of an instantaneous rise time suggests that ESA is the main UC mechanism. However, the fact that the emission lifetime is much longer than the intrinsic one, τ_0 , indicates that the ETU mechanism contributes to populate these energy levels.

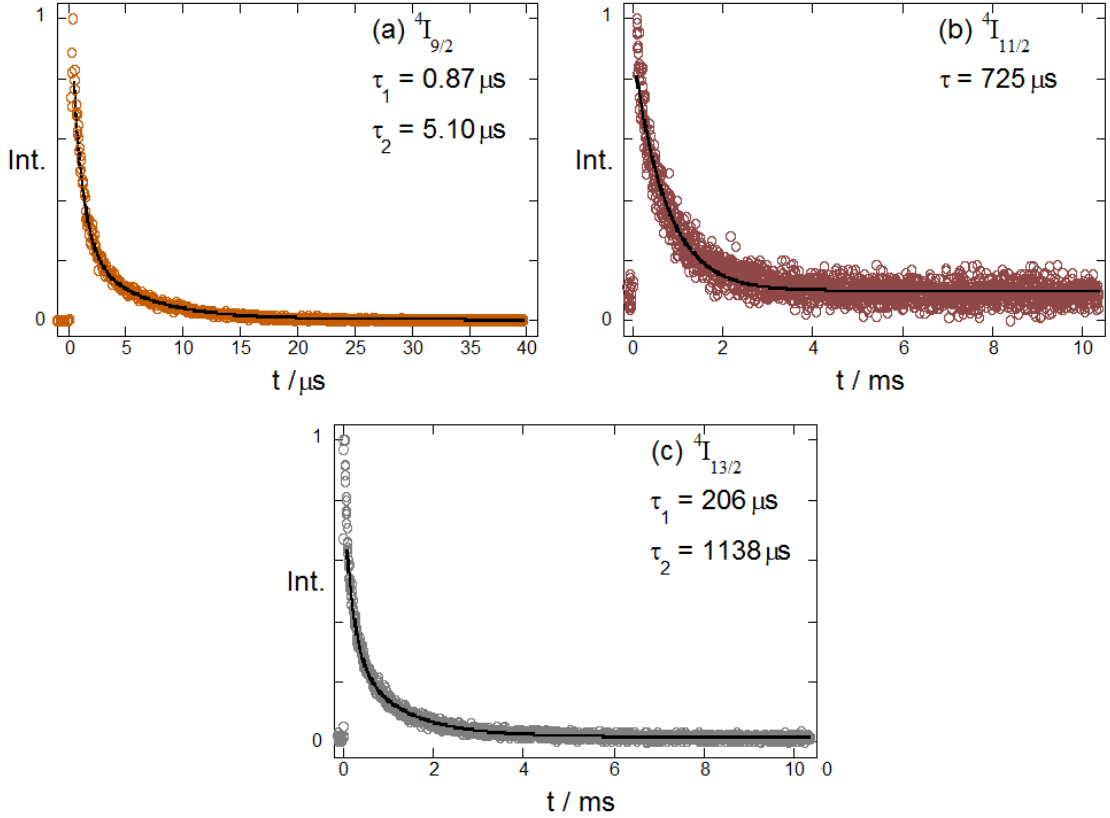


Figure 3.22: Decay curves of the Er^{3+} emission intensity from the ${}^4I_{9/2}$ at 820 nm after short pulsed excitation into the ${}^4I_{9/2}$ (a), ${}^4I_{11/2}$ (b), and ${}^4I_{13/2}$ (c) levels. Note the different time scale.

The emission at 670.1 nm from the ${}^4F_{9/2}$ level under direct excitation at 659 nm (Fig. 3.23(a)) shows a double exponential decay behavior ($\tau_1 = 13.97 \pm 0.15 \mu\text{s}$, $\tau_2 = 67.20 \pm 0.14 \mu\text{s}$). Again, non-radiative processes help to shorten the lifetime of the ${}^4F_{9/2}$ level in a $\text{Gd}_2\text{O}_2\text{S}:\text{Er}^{3+}(10\%)$ sample under direct excitation in comparison with the intrinsic lifetime, $\tau_0 = 100 \pm 1 \mu\text{s}$ (Table 1).

An initial rise of $\tau_R = 26.5 \pm 0.8 \mu\text{s}$ followed by a $\tau_D = 1.098 \pm 0.002 \text{ ms}$ decay is found upon excitation into the ${}^4I_{9/2}$ excited state at 805 nm (Fig. 3.23(b)). These values were obtained after fitting to a Vial's type equation (eq. (15)). The intense laser light masked luminescence at the very first instants, so it is not possible to distinguish whether luminescence starts from zero or not (in other words, which is the dominant mechanism).

Upon excitation into the ${}^4I_{11/2}$ level at 980.5 nm (Fig. 3.23(c)), a rising part ($\tau_R = 51.7 \pm 0.4 \mu\text{s}$) starting from zero precedes the decay ($\tau_D = 816 \pm 2 \mu\text{s}$), indicating a dominant ETU mechanism. This is also the case when exciting into the first excited state, ${}^4I_{13/2}$, at 980.5 nm (Fig. 3.23(d)), although longer rise and decay times are observed ($\tau_R = 113.4 \pm 1.3 \mu\text{s}$, $\tau_D = 1.096 \pm 0.005 \text{ ms}$). This reflects the long lifetime of the intermediate reservoir state.

The UC emission lifetime is much longer than the lifetime measured under direct excitation, which means that ETU continues populating the emitting level after the excitation pulse.

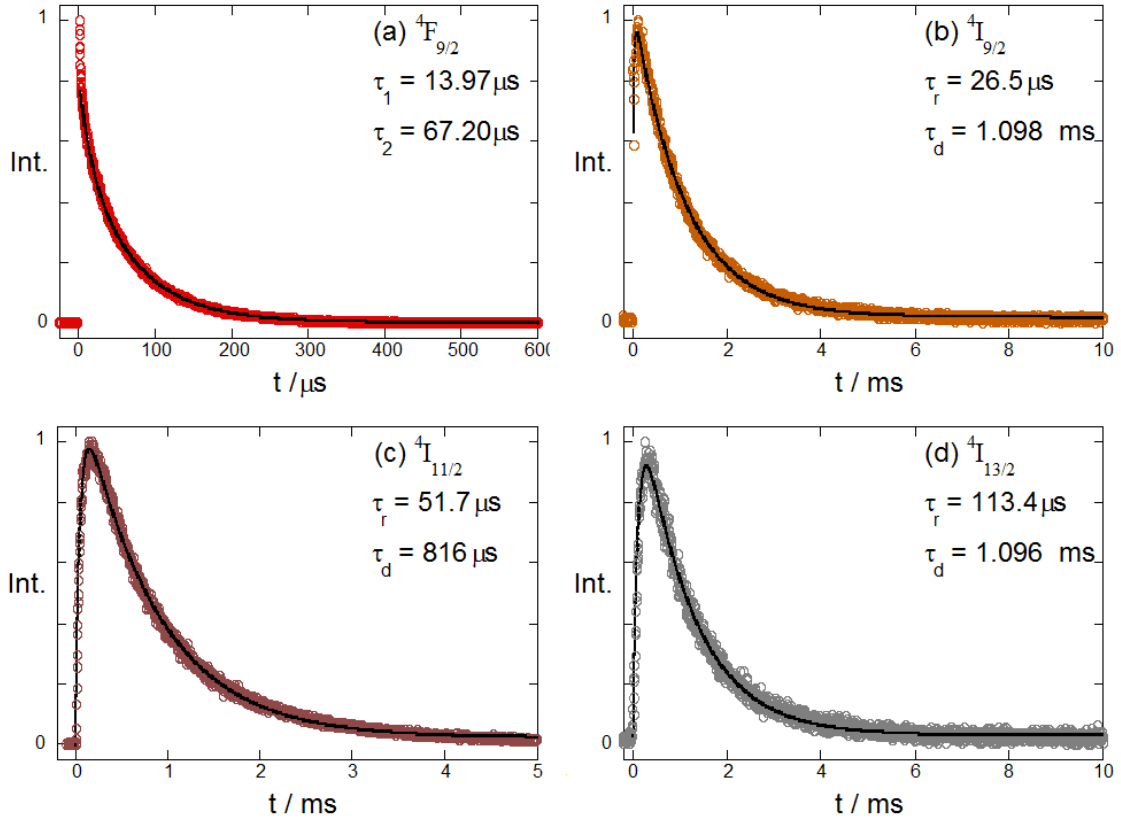


Figure 3.23: Decay curves of the Er^{3+} emission intensity from the ${}^4F_{9/2}$ at 670.1 nm after short pulsed excitation into the ${}^4F_{9/2}$ (a), ${}^4I_{9/2}$ (b), ${}^4I_{11/2}$ (c), and ${}^4I_{13/2}$ (d) levels. Note the different time scale.

The emission at 554 nm from the ${}^4S_{3/2}$ level under direct excitation at 523 nm (Fig. 3.24(a)) shows a bi-exponential decay ($\tau_1 = 2.476 \pm 0.012 \mu\text{s}$, $\tau_2 = 8.7 \pm 0.2 \mu\text{s}$). If we compare this with the intrinsic lifetime of the ${}^4S_{3/2}$ state, $\tau_0 = 560 \pm 20 \mu\text{s}$, it becomes evident that non-radiative processes contribute to de-populate this state.

Upon excitation into the ${}^4F_{9/2}$ level at 679 nm (Fig. 3.24(b)), a double exponential decay behavior ($\tau_1 = 62.81 \pm 0.16 \mu\text{s}$, $\tau_2 = 797 \pm 6 \mu\text{s}$) was observed, which corresponds to an ESA up-conversion process. The same occurred for excitation into the ${}^4I_{9/2}$ state at 805 nm (Fig. 3.24(c)) ($\tau_1 = 259 \pm 3 \mu\text{s}$, $\tau_2 = 1.063 \pm 3 \text{ms}$) and into the ${}^4I_{11/2}$ state at 980.5 nm (Fig. 3.24(d)) ($\tau_1 = 81.6 \pm 0.7 \mu\text{s}$, $\tau_2 = 527 \pm 3 \mu\text{s}$).

Finally, excitation into the first excited state, ${}^4I_{13/2}$, at 1511 nm (Fig. 3.24(e)) shows a rise of $\tau_R = 269 \pm 8 \mu\text{s}$ followed by a $\tau_D = 1.245 \pm 14 \text{ms}$ decay. This emission is mainly due to an ETU mechanism, although ESA also contributes to UC luminescence [4].

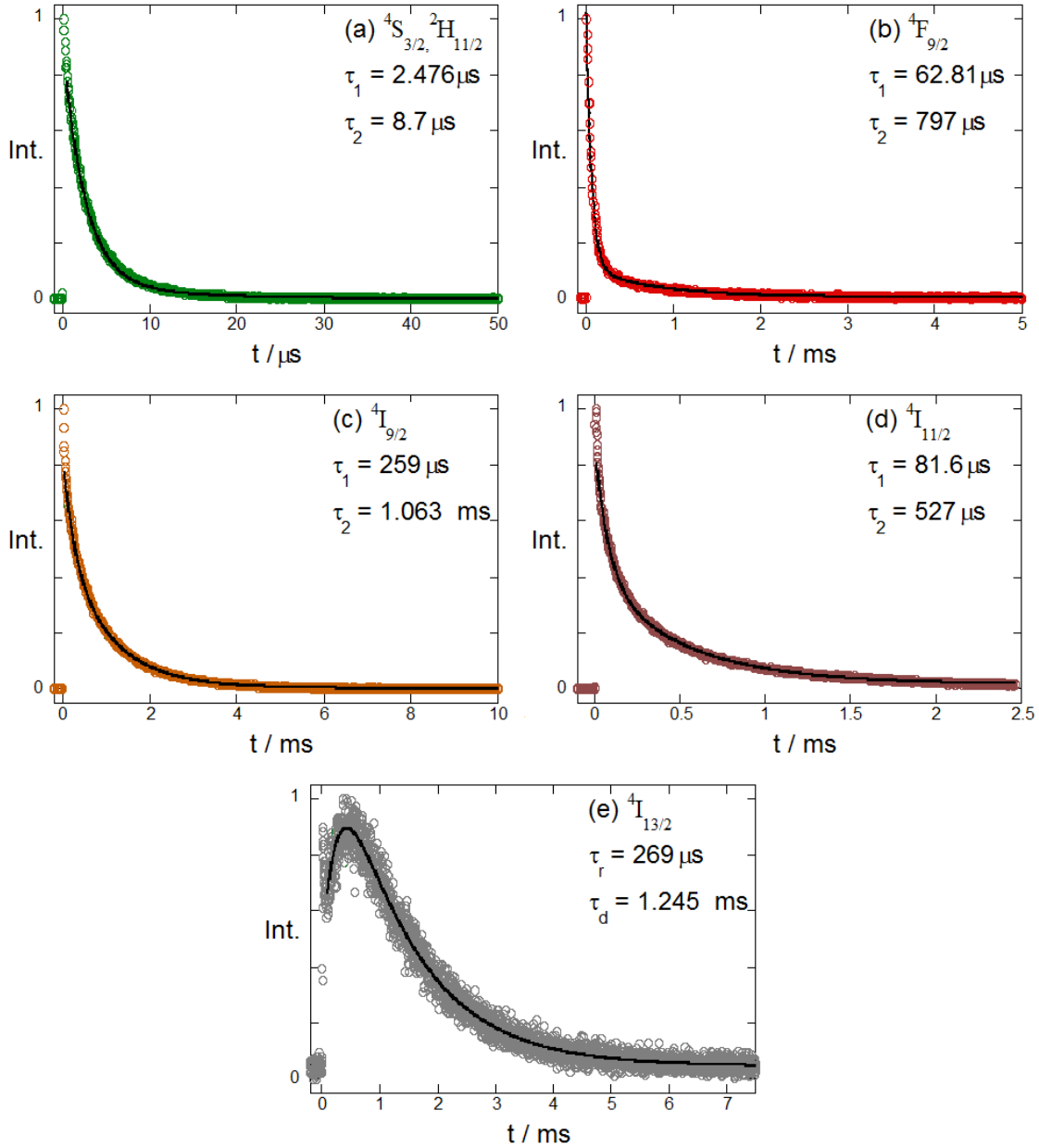


Figure 3.24: Decay curves of the Er^{3+} emission intensity from the $^4\text{S}_{3/2}$ at 554 nm after short pulsed excitation into the $^4\text{S}_{3/2} - ^2\text{H}_{11/2}$ (a), $^4\text{F}_{9/2}$ (b), $^4\text{I}_{9/2}$ (c), $^4\text{I}_{11/2}$ (d), and $^4\text{I}_{13/2}$ (e) levels. Note the different time scale.

The emission at 410 nm from the $^2\text{H}_{9/2}$ multiplet under direct excitation shows a very short lifetime which was not measured due to setup limitations.

When exciting into the $^4\text{S}_{3/2}$ level at 523 nm (Fig. 3.25(a)), a bi-exponential decay ($\tau_1 = 0.822 \pm 0.011 \mu\text{s}$, $\tau_2 = 6.29 \pm 0.12 \mu\text{s}$) was recorded. Excitation into the $^4\text{F}_{9/2}$ level at 679 nm (Fig. 3.25(b)) gives rise to a single exponential decay ($\tau = 92.0 \pm 0.8 \mu\text{s}$). Then, a two exponential decay behavior was recorded for excitation into the $^4\text{I}_{9/2}$ state at 805 nm (Fig. 3.25(c)) ($\tau_1 = 0.617 \pm 0.015 \mu\text{s}$, $\tau_2 = 3.05 \pm 0.05 \mu\text{s}$) and also for excitation into the $^4\text{I}_{11/2}$ state at 980.5 nm (Fig.

3.25(d)) ($\tau_1 = 110 \pm 2 \mu\text{s}$, $\tau_2 = 426 \pm 9 \mu\text{s}$). Finally, a single exponential decay ($\tau = 668 \pm 8 \mu\text{s}$) was observed under excitation into the first excited state, $^4I_{13/2}$, at 1511 nm (Fig. 3.25(e)).

No rise time was observed for any of the excitation wavelengths. However, we cannot assure that the main UC mechanism is ESA since we were not able to record luminescence that changed too fast (either a rise or a decay), since the maximum temporal resolution of the setup used is 5 ns.

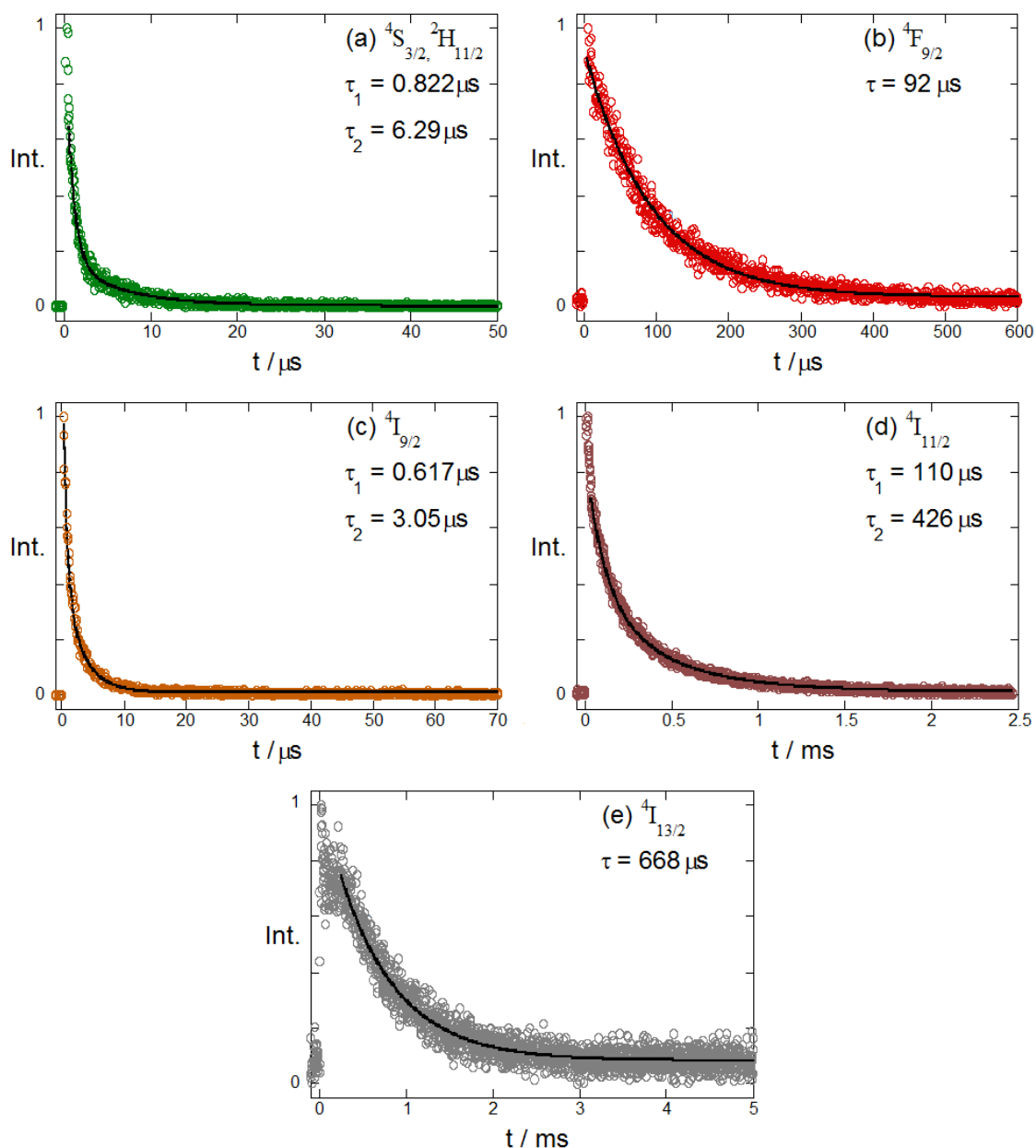


Figure 3.25: Decay curves of the Er^{3+} emission intensity from the $^2H_{9/2}$ at 410 nm after short pulsed excitation into the $^4S_{3/2} - ^2H_{11/2}$ (a), $^4F_{9/2}$ (b), $^4I_{9/2}$ (c), $^4I_{11/2}$ (d), and $^4I_{13/2}$ (e) levels. Note the different time scale.

The different UC lifetime measured for each excitation wavelength is connected both with the intrinsic lifetime of the emitting state and the lifetime of the intermediate reservoir state.

All the lifetime results are summarized in the following table:

Emitting state	Excitation into				
	${}^4I_{13/2}$	${}^4I_{11/2}$	${}^4I_{9/2}$	${}^4F_{9/2}$	${}^4S_{3/2}$
${}^4I_{9/2}$	$\tau_1 = 206 \mu\text{s}$ $\tau_2 = 1.138 \text{ ms}$	$\tau = 725 \mu\text{s}$	$\tau_1 = 0.87 \mu\text{s}$ $\tau_2 = 5.10 \mu\text{s}$		
${}^4F_{9/2}$	$\tau_R = 113.4 \mu\text{s}$ $\tau_D = 1.096 \text{ ms}$	$\tau_R = 51.7 \mu\text{s}$ $\tau_D = 816 \mu\text{s}$	$\tau_R = 26.5 \mu\text{s}$ $\tau_D = 1.098 \text{ ms}$	$\tau_1 = 13.97 \mu\text{s}$ $\tau_2 = 67.20 \mu\text{s}$	
${}^4S_{3/2}$	$\tau_R = 269 \mu\text{s}$ $\tau_D = 1.245 \text{ ms}$	$\tau_1 = 81.6 \mu\text{s}$ $\tau_2 = 527 \mu\text{s}$	$\tau_1 = 259 \mu\text{s}$ $\tau_2 = 1.063 \text{ ms}$	$\tau_1 = 62.81 \mu\text{s}$ $\tau_2 = 797 \mu\text{s}$	$\tau_1 = 2.476 \mu\text{s}$ $\tau_2 = 8.7 \mu\text{s}$
${}^2H_{9/2}$	$\tau = 668 \mu\text{s}$	$\tau_1 = 110 \mu\text{s}$ $\tau_2 = 426 \mu\text{s}$	$\tau_1 = 0.617 \mu\text{s}$ $\tau_2 = 3.05 \mu\text{s}$	$\tau = 92.0 \mu\text{s}$	$\tau_1 = 0.822 \mu\text{s}$ $\tau_2 = 6.29 \mu\text{s}$

Table 2: Normal and UC lifetimes of Er^{3+} excited states in $\text{Gd}_2\text{O}_2\text{S: Er}^{3+}(10\%)$ measured after short-pulsed excitation into the emitting level and other lower lying states.

3.4.1 Temperature dependence of the lifetime of some Er^{3+} excited states

The lifetime of the ${}^4F_{9/2}$ and ${}^4S_{3/2}$ excited states in $\text{Gd}_2\text{O}_2\text{S: Er}^{3+}(10\%)$ under direct excitation and upon pulsed excitation into the ${}^4I_{11/2}$ level at 980 nm was measured at different temperatures.

It is important to note that in contrast with the OPO system, which allows excitation with a pulse width below 10 ns, the pulsed xenon lamp of the FLS920 spectrofluorimeter works in the microsecond range. This is also the case when working under NIR excitation with the 980 nm laser diode. Longer excitation pulses affect considerably the population dynamics, that is, excitation, de-excitation and up-conversion processes.

In Fig. 3.26(a) the emission at 670 nm from the ${}^4F_{9/2}$ level under direct excitation at 659 nm shows a maximum decay lifetime at 125 K, $\tau_{125} = 119.5 \pm 0.1 \mu\text{s}$. Then, the red luminescence decays faster for higher temperatures, and the shortest lifetime, $\tau_{300} = 71.5 \pm 0.1 \mu\text{s}$, agrees well with $\tau_2 = 67.20 \pm 0.14 \mu\text{s}$ of the ${}^4F_{9/2}$ state under direct excitation (see Fig. 3.23(a)).

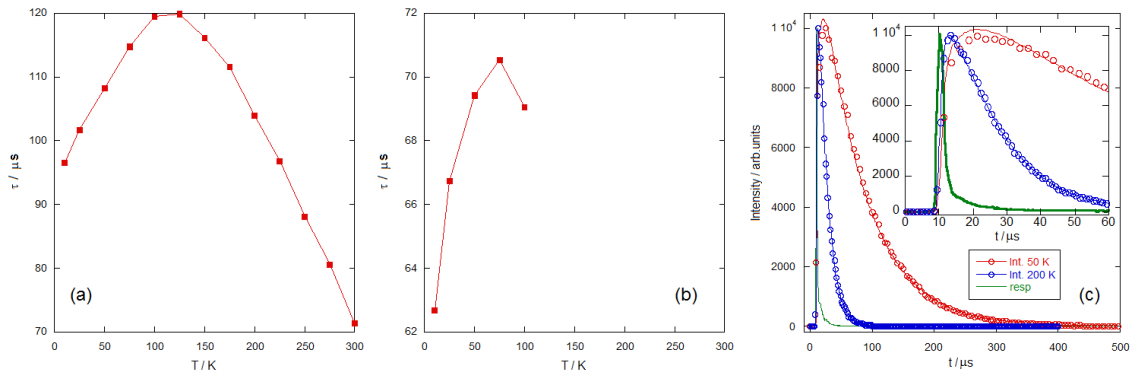


Figure 3.26: Temperature dependence of the lifetime of the $^4F_{9/2}$ (a) and $^4S_{3/2}$ (b) excited states in $\text{Gd}_2\text{O}_2\text{S}:\text{Er}^{3+}$ (10%) under direct excitation. Lines are guides for the eye. (c) Temporal evolution of the green emission under direct excitation of the $^4S_{3/2}$ state at 50 K and 200 K, and response curve of the detector. The inset shows the peaks amplified.

The temporal evolution of the green emission from the $^4S_{3/2}$ excited state at 555 nm under direct excitation at 523 nm was measured. However, the lifetime could only be accurately determined for temperatures below 100 K as it is shown in Fig. 3.26(b). The response time of the detector is comparable with the state lifetime at higher temperatures, which affects the time dependence of the emission. Remember that $\langle\tau\rangle = 8.75 \mu\text{s}$ was the average lifetime calculated for this level under direct excitation in Fig. 3.23(a). In Fig. 3.26(c) a comparison between the emission decay at 50 K and 200 K is presented.

In Fig. 3.27(a, b) the temperature dependence of the UC lifetime of the $^4F_{9/2}$ and $^4S_{3/2}$ excited states under NIR excitation is shown. For both the red and the green emissions the UC lifetime is of the order of few ms, one order of magnitude longer than under direct excitation. This lengthening indicates that the luminescence decay is affected by the long lifetime of the $^4I_{11/2}$ level that acts as a reservoir for the UC emission, which is shown in Fig. 3.27(c), and also that ETU is the dominant UC mechanism.

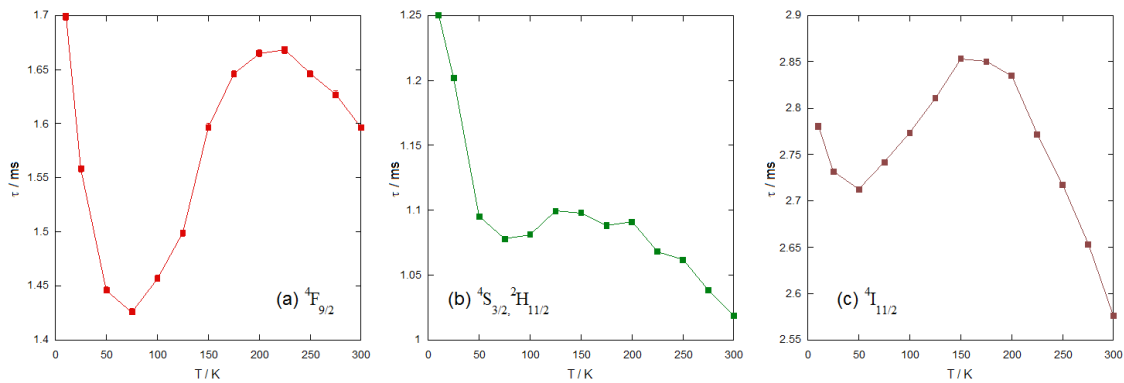


Figure 3.27: Temperature dependence of the UC lifetime of the $^4F_{9/2}$ (a) and $^4S_{3/2}$ (b) excited states in $\text{Gd}_2\text{O}_2\text{S}:\text{Er}^{3+}$ (10%) under 980 nm excitation. Temperature dependence of the lifetime of the $^4I_{11/2}$ (c) level under direct excitation. Lines are guides for the eye.

ETU is also temperature dependent. For red and green UC emission, the shortest lifetime is found at the minimum temperature, 10 K. And then, the temperature dependence shows a similar behavior to that of the state into which excitation took place, ${}^4I_{11/2}$.

The fact that the UC lifetime at 300 K is around twice the lifetime determined in Fig. 3.23(c) and Fig. 3.24(d) for the ${}^4F_{9/2}$ and ${}^4S_{3/2}$ states under 980 nm excitation is connected with the excitation pulse length, as mentioned before.

3.4.2 Rate equations

The solution of simple rate equations is the appropriate way to interpret lifetime measurements. However, the amount of parameters that must be tuned in the simulation makes it very complex.

The green UC emission from the ${}^4S_{3/2}$ states under 980 nm excitation into the ${}^4I_{11/2}$ state at room temperature has been simulated. In Fig. 3.28 an energy level diagram of Er^{3+} ions shows the transitions responsible for this emission. Also, states have been labeled in accordance with the subindex of the parameters in the rate equations.

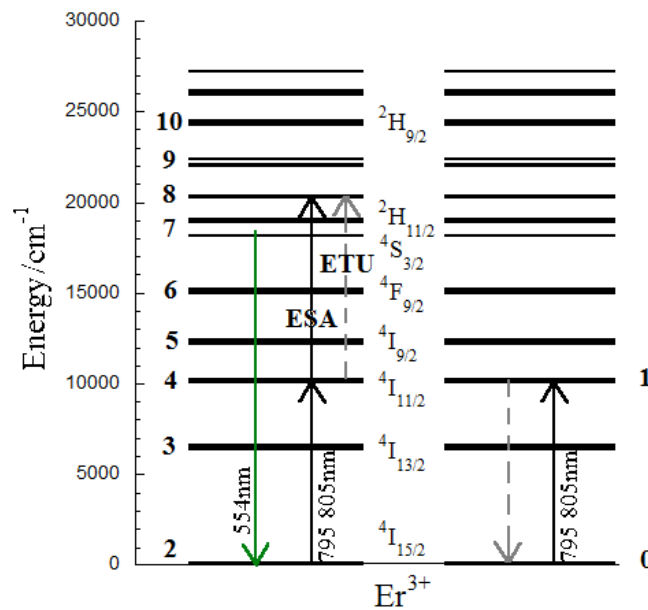


Figure 3.28: Energy level diagram of Er^{3+} ions showing the excitation and the emission wavelength. The ESA and ETU mechanisms responsible for this up-conversion luminescence are also shown.

We have used the following rate equations, where G is the pump rate, N_i is the population of the i state, $K_i = \tau_i^{-1}$ is the rate constant of that state, β_{ij} is the branching ratio of the transition from state i to state j , and W_{ij} is the energy transfer rate from state i to state j .

$$\begin{aligned} \frac{dN_0}{dt} &= -GN_0 + K_1N_1 + W_{14}N_1N_4 \\ \frac{dN_1}{dt} &= +GN_0 - K_1N_1 - W_{14}N_1N_4 \\ \frac{dN_2}{dt} &= -GN_0 + K_3N_3 + \beta_{42}K_4N_4 + \beta_{52}K_5N_5 + \beta_{62}K_6N_6 + \beta_{72}K_7N_7 \\ \frac{dN_3}{dt} &= -K_3N_3 + \beta_{73}K_7N_7 + \beta_{43}K_4N_4 \\ \frac{dN_4}{dt} &= +GN_0 - G \text{ESA} N_4 - W_{14}N_1N_4 + \beta_{54}K_5N_5 - (\beta_{43} + \beta_{42})K_4N_4 \\ \frac{dN_5}{dt} &= -(\beta_{54} + \beta_{52})K_5N_5 + \beta_{65}K_6N_6 \\ \frac{dN_6}{dt} &= \beta_{76}K_7N_7 - (\beta_{62} + \beta_{65})K_6N_6 \\ \frac{dN_7}{dt} &= +G \text{ESA} N_4 - (\beta_{72} + \beta_{73} + \beta_{76})K_7N_7 + W_{14}N_1N_4 \end{aligned}$$

The τ_i used for each state is the intrinsic lifetime shown in Table 1. The value of the other parameters has been tuned until a perfect match between the experimental results and the simulation was achieved.

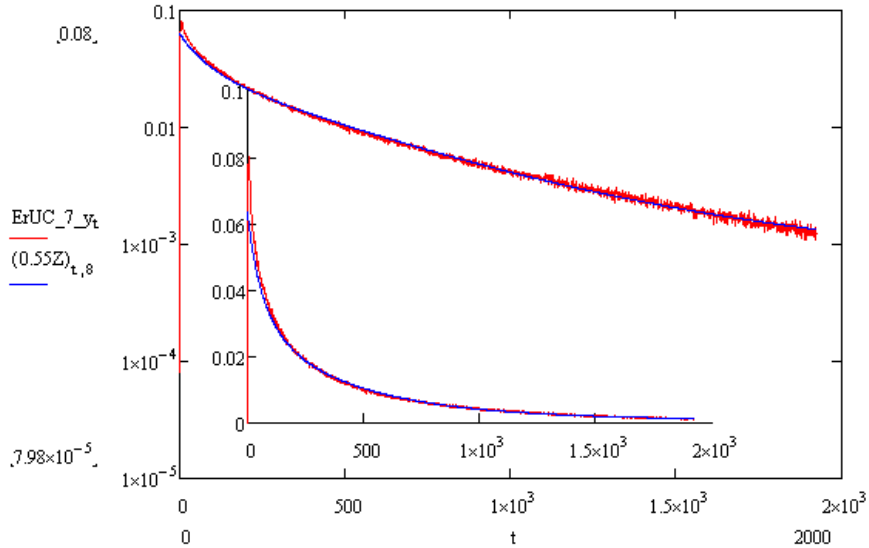


Figure 3.29: UC lifetime of the ${}^4S_{3/2}$ under 980 nm excitation into the ${}^4I_{11/2}$ state in logarithmic and linear (inset) scale. Measurements are shown in red while the blue line corresponds to the simulation. Note the scale in the x-axis corresponds to the number of points used for the simulation, not to time units.

4 CONCLUSIONS

Herein the most relevant conclusions of this work are summarized:

- The maximum phonon energy of the lattice, $\hbar\omega_{max} \approx 450 \text{ cm}^{-1}$, has been determined through a Raman spectrum obtained under 488 nm excitation.
- The peaks in the absorption (reflectance), excitation and emission spectra could be assigned by comparison with the Dieke diagram. Also, the fact that bands show sharp lines confirms that in RE^{3+} f-f transitions are weakly affected by the crystal field.
- The population of the ${}^2H_{11/2}$ and ${}^4S_{3/2}$ states is thermally coupled. This has been confirmed by fitting the ratio between the emission intensity from both energy levels versus temperature to an exponential curve, according with the Boltzmann population factor. As a result, an energy difference of about 700 cm^{-1} between these states was determined.
- The effect of the crystal-field on two Er^{3+} excited states, ${}^4S_{3/2}$ and ${}^4F_{9/2}$, and the ground state, ${}^4I_{15/2}$, was studied. While the former showed no splitting at all, for the first time an energy splitting of $\Delta E = 240 \text{ cm}^{-1}$ and $\Delta E = 453 \text{ cm}^{-1}$ was determined for the ${}^4F_{9/2}$ excited state and the ${}^4I_{15/2}$ ground state, respectively.
- Up-conversion emission around 410 nm (blue), 554 nm (green), 670 nm (red) and 820 nm (NIR) was achieved working with various excitation energies. In fact, blue UC luminescence was observed under excitation into five different lower Er^{3+} excited states, which had never been observed before in any UC material.
- The time dependence of the UC luminescence using short pulsed-excitation allowed us to identify the dominant UC mechanism. A rise followed by a decay or a pore decay with an instantaneous rise points to ETU or ESA, respectively, as the main up-converting process.
- The lengthening of the UC lifetime compared to the lifetime under direct excitation indicates that the former is affected by the lifetime of the intermediate state that feeds the UC emission due to an ETU contribution.
- Lifetime concentration dependence, comparing 0.1% Er^{3+} and 10% Er^{3+} pointed out that the contribution of non-radiative processes (multi-phonon relaxation, migration and up-conversion mechanisms) to de-populate Er^{3+} excited states makes the lifetime under direct excitation for 10% Er^{3+} concentration shorter than for very low concentrations.

References

- [1] F. Auzel. *Acad. Sci.* 263 B: 765, 1966.
- [2] F. Auzel. *Acad. Sci.* 262: 1016, 1966.
- [3] 22 V.V. Ovsyankin, P.P. Feofilov. *Jetp. Lett.* 3: 322, 1966.
- [4] R. Martín-Rodríguez, S. Fischer, A. Ivaturi, B. Froehlich, K. W. Krämer, J. C. Goldschmidt, B. S. Richards, and A. Meijerink. Highly Efficient IR to NIR Upconversion in $\text{Gd}_2\text{O}_2\text{S}:\text{Er}^{3+}$ for Photovoltaic Applications. *Chem. Mater.*, 25:1912–1921, 2013.
- [5] W.G.J.H.M. van Sark, A. Meijerink and R.E.I. Schropp. *Solar Spectrum Conversion for Photovoltaics Using Nanoparticles*, Chapter 1 in Third Generation Photovoltaics. Dr.Vasilis Fthenakis (Ed.), I nTech, 2012.
- [6] S.Hao, G. Chen, and C. Yang. Sensing Using Rare-Earth-Doped Upconversion Nanoparticles. *Theranostics*, 3(5):331-345, 2013.
- [7] R. Naccache, E. Martín Rodríguez, N.Bogdan, F. Sanz-Rodríguez, M.C. Iglesias de la Cruz, A. Juarranz de la Fuente, F. Vetrone, D. Jaque, J. García Solé and J.A. Capobianco. High Resolution Fluorescence Imaging of Cancers Using Lanthanide Ion-Doped Upconverting Nanocrystals. *Cancers*, 4:1067-1105, 2012.
- [8] M. Nyk, R. Kumar, T.Y. Ohulchansky, E.J. Bergey, and P.N. Prasad. High contrast in vitro and in vivo Photoluminescence bioimaging using Near Infrared to Near Infrared Up-Conversion in $\text{Tm}^{3+}, \text{Yb}^{3+}$ doped Fluoride Nanophosphors. *Nano Lett.*, 8(11):3834–3838, 2008.
- [9] J.F. Suyver, A. Aebischer, D. Biner, P. Gerner, J. Grimm, S. Heer, K.W. Krämer, C. Reinhard, and H.U. Güdel. Novel materials doped with trivalent lanthanides and transition metal ions showing near-infrared to visible photon upconversion. *Opt. Mater.*, 27:1111-1130, 2005.
- [10] B.H. Bransden and C.J. Joachain. *The Physics of Atoms and Molecules*. Longman, London, Second Edition 2003.
- [11] O.L. Malta and L.D. Carlos. Intensities of 4f-4f transitions in glass materials. *Quim. Nova*, 26(6):889-895, 2003.
- [12] R. Martín-Rodríguez. *Síntesis y caracterización de nanopartículas de óxidos y fluoruros*. Master thesis, Universidad de Cantabria.
- [13] G.H. Dieke and H.M. Crosswhite. The Spectra of the Doubly and Triply Ionized Rare Earths. *Applied Optics*, 2(7):675-686, 1963.
- [14] C. Renero-Lecuna. *Dependencia de la luminiscencia del $\text{NaYF}_4:\text{Er}^{3+}, \text{Yb}^{3+}$ con la energía de excitación, la presión y la temperatura*. Master thesis, Universidad de Cantabria, 2009-2010.
- [15] J. García Solé, L. E. Bausá, and D. Jaque. *An Introduction to the Optical Spectroscopy of Inorganic Solids*. John Wiley & Sons, 2005.

- [16] B.G. Wybournem. The fascination of the rare earths - then, now and in the future. *Journal of Alloys and Compounds*, 380: 96–100, 2004.
- [17] T.C. Brunold and H.U. Güdel. *Luminescence Spectroscopy*, pp. 259–306 in Inorganic electronic structure and spectroscopy. Eds. E. I. Solomon and A. B. P. Lever, Wiley, New York, 1999.
- [18] F. Auzel. Upconversion and Anti-Stokes Processes with f and d Ions in Solids. *Chem. Rev.*, 104(1):139-174, 2004.
- [19] G.A. Kumar, M. Pokhrel, and D.K. Sardar. Intense visible and near infrared upconversion in M_2O_2S : Er (M=Y, Gd, La) phosphor under 1550 nm excitation. *Mater.Lett.*, 68:395-398, 2012.
- [20] Jing Huang, Yanhua Song, Ye Sheng, Keyan Zheng, Hongbo Li, Hongguang Zhang, Qisheng Huo, Xuechun Xu, Haifeng Zou. $Gd_2O_2S:Eu^{3+}$ and $Gd_2O_2S:Eu^{3+}/Gd_2O_2S$ hollow microspheres: Solvothermal preparation and luminescence properties. *Journal of Alloys and Compounds*, 532: 34-40, 2012.
- [21] P.N. Yocom, J.P. Wittke, and I. Ladany. Rare-earth-doped oxysulfides for GaAs-pumped luminescent devices. *Metallurgical Transactions*, 2:763-767, 1971.
- [22] G.A. Kumar, M. Pokhrel, A. Martinez, R.C. Dennis, I.L. Villegas, and D.K. Sardar. Synthesis and spectroscopy of color tunable $Y_2O_2S:Yb^{3+},Er^{3+}$ phosphors with intense emission. *Journal of Alloys and Compounds*, 513:559-565, 2012.
- [23] M. Fox. *Optical Properties of Solids*. Oxford University Press, 2001.
- [24] P. Villanueva-Delgado. *Caracterización del $NaYF_4$ impurificado con Yb^{3+} y Tm^{3+} y sus potenciales aplicaciones en biomedicina*. Master thesis, Universidad de Cantabria, 2011-2012.
- [25] http://www.nanobase.co.kr/application/raman_spectro.php (July 27th, 213)
- [26] Yu.V.Orlovskii, T.T. Basiev, K.K. Pukhov, M.V. Polyachenkova, P.P. Fedorov, O.K. Alimov, E.I. Gorokhova, V.A. Demidenko, O.A. Khristich and R.M. Zakalyukin. Oxysulfide optical ceramics doped by Nd^{3+} for one micron lasing. *J. Lumin.*, 125: 201-215, 2007.
- [27] T.T. Basiev, V.A. Demidenko, K.V. Dykel'skii, P.P. Fedorov, E.I. Gorokhova, I.A. Mironov, Yu.V. Orlovskii, V.V. Osikoand A.N. Smirnov. *Optical Fluoride and Oxysulfide Ceramics: Preparation and Characterization*, Chapter 3 in Developments in ceramic materials research. Nova Science Publishers, 2007.
- [28] G.V. Anan'eva, E.I. Gorokhova, V.A. Demidenko, V. A. Parfinskii, and O.A. Khristich. Optical properties of Gd_2O_2S -based ceramic. *J. Opt. Technol.*, 72(1):58-61, 2005.